Fabrication of Anti-reflective and Imaging Nanostructured Optical Elements

by

Hyungryul Choi

B.S., Korea Advanced Institute of Science and Technology (2009)

Submitted to the Department of Mechanical Engineering
in partial fulfillment of the requirements for the degree of

Master of Science in Mechanical Engineering

at the

MASSACHUSETTS INSTITUTE OF TECHNOLOGY

June 2011

Author ....
Department of Mechanical Engineering
May 19, 2011

Certified by..
George Barbastathis
Professor, Mechanical Engineering
Thesis Supervisor

Accepted by ....
David E. Hardt
Chairman, Department Committee on Graduate Theses

Fabrication of Anti-reflective and Imaging Nanostructured Optical Elements

by

Hyungryul Choi

Submitted to the Department of Mechanical Engineering
on May 19, 2011, in partial fulfillment of the
requirements for the degree of
Master of Science in Mechanical Engineering

Abstract

Moth eyes minimize reflection over a broad band of angles and colors and lotus leaves minimize wetting over a broad range of breakthrough pressures by virtue of subwavelength structures patterned on their respective surfaces; similar examples of organisms exploiting geometry to attain properties unavailable in bulk materials are abundant in nature. These instances have inspired applications to man-made structures, collectively known as functional materials: for example, self-cleaning/anti-fogging surfaces, and solar cells with increased efficiency. I fabricated a functional surface where both wetting and reflectivity are controlled by geometry. Using a periodic array of subwavelength-sized high aspect ratio cones, patterned on glass and coated with optimized surfactants, I have experimentally shown that we can significantly enhance transmission from the surfaces of a glass slab, and at the same time make the surfaces either superhydrophobic or superhydrophilic, depending on the applications, such as antifogging and self-cleaning glass. Novel lithographic techniques result in high patterning accuracy over large surface areas, and is easily adaptable to nanoimprinting for future mass replication. In addition, an all-dielectric subwavelength-patterned Luneburg lens was fabricated for operation at free-space wavelength of $\lambda = 1.55\ \mu$m.

Thesis Supervisor: George Barbastathis
Title: Professor, Mechanical Engineering

Acknowledgments

First of all I would like to thank my research advisor Professor George Barbastathis. The guidance and support he provided were invaluable to me.

I also thank Dr. Chih-Hao Chang, Dr. Se Young Yang, and Satoshi Takahashi for the knowledge and tremendous help.

I also would like to thank my collaborators, Kyoo-Chul Park, Professor Gareth H. McKinley, and Professor Robert E. Cohen. Without their help, I cannot make a success on fabricating the multifuctional glass.

The Nanostructures Laboratory (NSL) and Microsystems Technology Lab (MTL) at MIT, as well as the Center for Nanoscale Systems (CNS) at Harvard were great facilities to work in with great staff maintaining the environment and the machines. Especially James Daley and Mark Mondol gave me tremendous help in fabricating devices.

Also, I am also grateful to all members in 3D Optical System Group. I really enjoyed all discussion in our office.

Lastly, I would like to thank my parents and sister for supporting me all the way through my career at MIT.

Contents

List of Figures

List of Tables

Chapter 1

Introduction

Numerous studies on natural surfaces such as body parts of animals and plant leaves have revealed the complementary role of material property and texture on surface functionality resulted from the adaptations to different environments [1, 2, 3]. These analyses of the each functional surface have led to the creation of artificial biomimetic surfaces emulating anti-reflective property of moth eyes [4] and self-cleaning effect of lotus leaves [5, 6, 7]. However, it has recently been recognized by researchers that many biological surfaces have been evolved to possess multiple fascinating functions ranging from optical properties to wetting on a single surface [8].

Many engineering applications including energy harvesting and utilization have also been highlighted to reinforce the necessity of developing multi-functional surfaces that go beyond emulating individual characteristics of natural surfaces. For example, the collecting efficiency of a photovoltaic solar cell is highly influenced by both surface dust contamination and Fresnel reflection losses [9]. The collection efficiency could be improved by utilizing biomimetic surfaces with both enhanced self-cleaning and anti-reflection properties. As an alternative example, electric vehicles designs seek to reduce power consumption by reducing the need for operating internal window heater by implementing anti-fogging function on the inside of the windshield. However, a coupled analysis and integrative design of wetting and optical functions have been rare and remained on the level of a simple pairwise combination of design consideration from two distinct fields.

In this work, by incorporating knowledge obtained from this combination of optics and wetting, artificial surfaces were fabricated while possessing highly robust superhydrophobicity or enhanced structural superhydrophilicity, depending on chemical treatment as well as broadband omnidirectional anti-reflectance, and near-lossless transparency that are superior to structures found in nature.

1.1 Bio-inspired Materials

Biological surfaces have evolved to optimize physicochemical properties and structures at the micro/nanoscale for a wide variety of functions, ranging from optical properties to wettability. Recently, researchers have recognized that many natural surfaces are not limited to a single function but Nature is an excellent architect to design and optimize surfaces for multiple purposes. In this section, biological surfaces and bio-inspired surfaces are examined.

1.1.1 Anti-reflective Surface

It is well known that such a surface with gradually varying index of refraction has suppressed Fresnel reflection [10, 11], allowing broadband wavelength light with wide incident angles is allowed to pass through these structures without reflection losses. Figure 1-1 explains the principle of reducing Fresnel reflection on an interface with optical impedance matching through gradient index.

Anti-reflective nipple arrays on ommatidial surfaces of a lepidopteran eye, which is an example of anti-reflective surfaces in biological creatures, are shown in Figure 1-2. Anti-reflective property of the surface due to the nanostructures enhances the photon collection efficiency of the visual system [12].

These anti-reflective surfaces using gradually varying index of refraction have been fabricated by two methods: multilayer evaporation of porous films [13] and subwavelength tapered nanostructures [14], as shown in Figure 1-3.

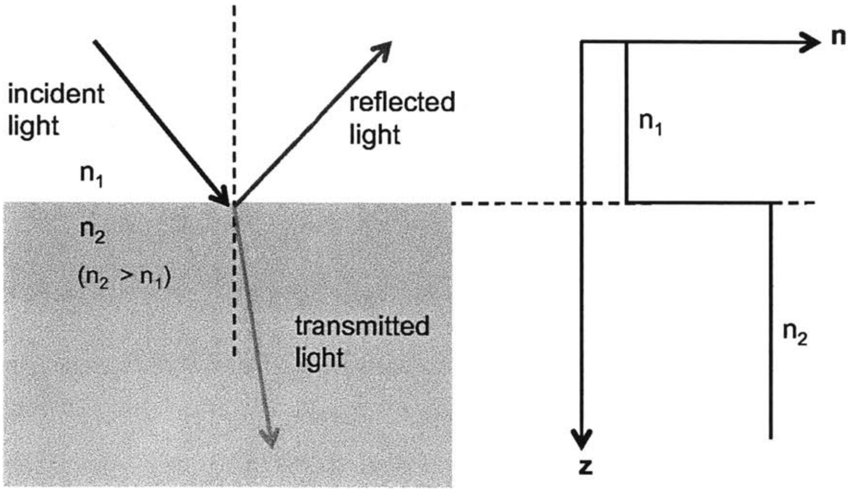

<Typical Fresnel Reflection on Optical Interface>

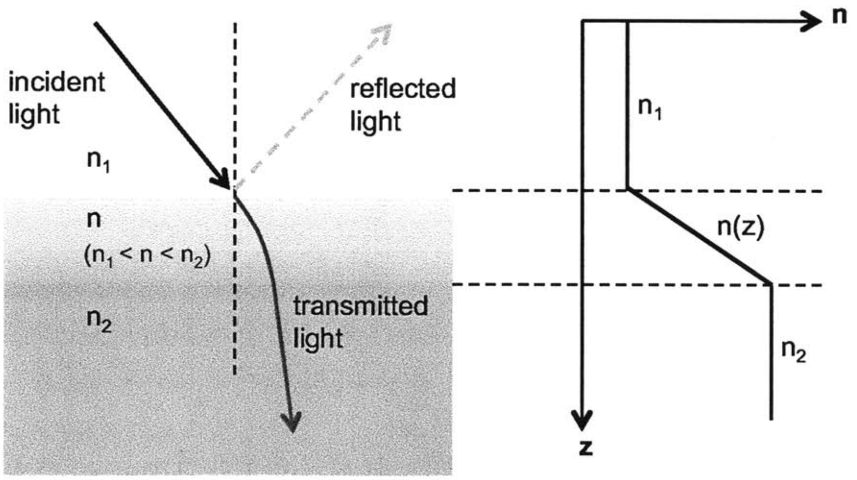

<Minimized Fresnel Reflection due to Gradient Index>

Figure 1-1: Principle of anti-reflective surface from gradient index of refraction

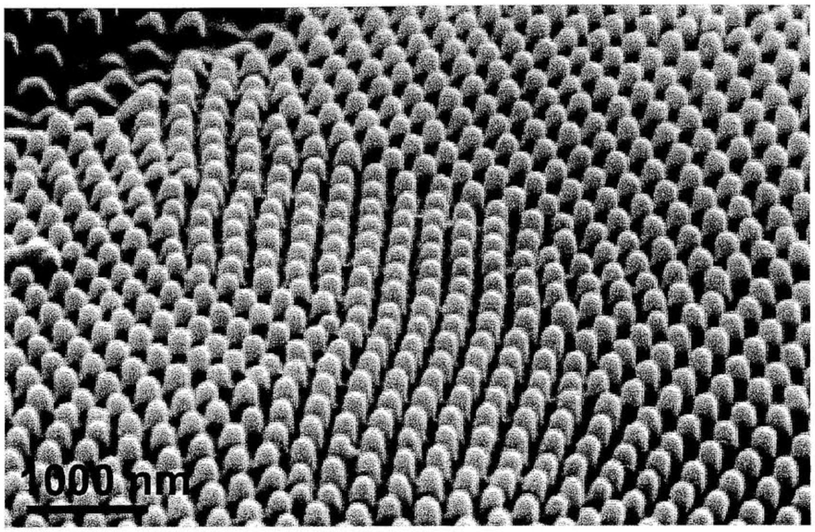

Figure 1-2: Subwavelength nanostructures on ommatidial surfaces of a lepidopteran eye [12]

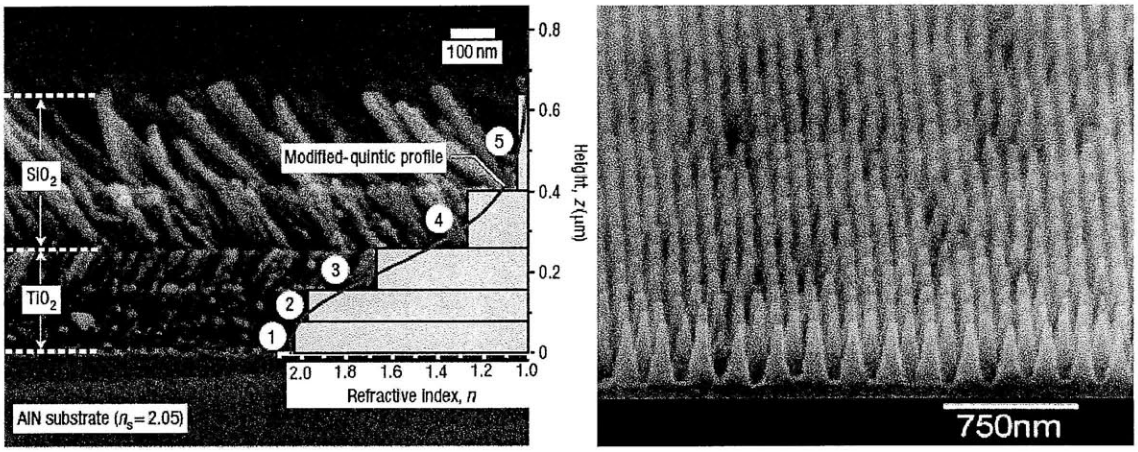

Multilayer Evaporation of Porous Films

Tapered Nanostructures

Figure 1-3: Two different fabrication methods of anti-reflective surfaces: multilayer evaporation of porous films [13] and subwavelength tapered nanostructures [14]

Especially subwavelength tapered structures have been widely developed years in order to fabricate anti-reflective surfaces. Due to the smaller size of the structures than wavelength of visible light, the structure behaves as an effective medium with gradually varying index of refraction, and Fresnel reflection from the surface minimizes. These nanostructured surfaces can be fabricated by existing fabrication methods, such as electron beam lithography [15], nanoimprint/polymer replication [16], deposition of multilayer porous films or chemical materials [13], and colloidal lithography [17, 18]. In this work, the tapered nanostructures are used for achieving anti-reflective and superhydrophobic/philic surface since those also acquire hierarchical roughness related to wetting properties.

1.1.2 Superhydrophobic and Superhydrophilic Surfaces

Lotus leaf is one of the most popular examples of superhydrophobic surfaces, which is defined to show, for water, equilibrium contact angles greater than 150° and contact angle hysteresis (i.e., difference between advancing contact angle and receding contact angle) less than 5°. Figure 1-4 demonstrates its self-cleaning effect. Superhydrophic surfaces inspired by Lotus leaf have been fabricated [5, 6, 7, 19], and have been studied for self-cleaning effect.

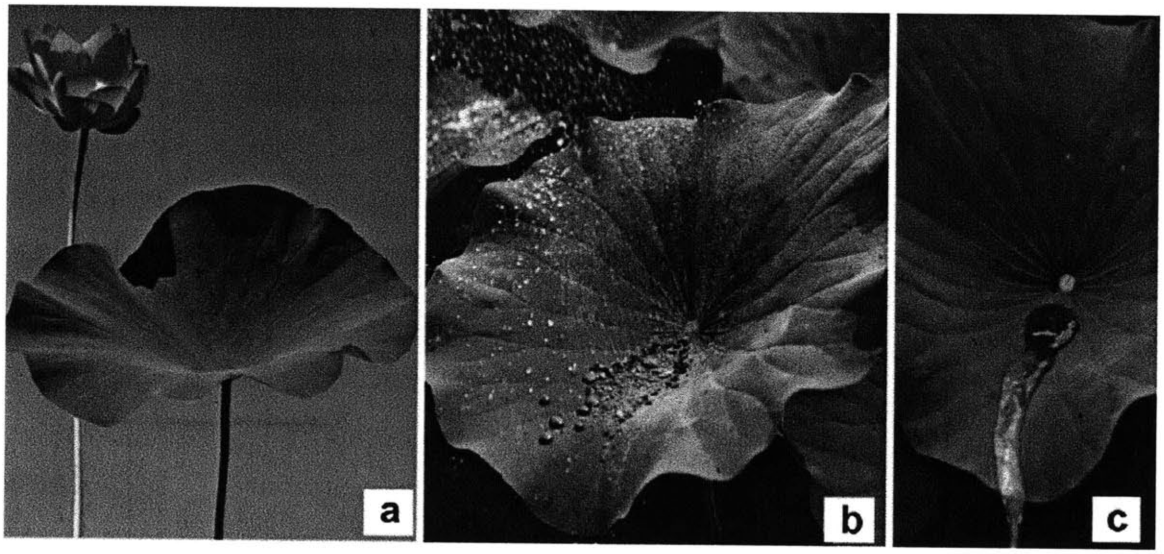

Figure 1-4: Lotus plant (Nelumbo nucifera) (a): self-cleaning effect from (b) to (c) [20]

On the other hand, superhydrophilic surfaces are defined to exhibit equilibrium contact angles less than 10°. Stenocara, one of the beetles in Namib Desert of southern Africa, collects water droplets by virtue of its surface consisting of alternating hydrophobic, wax-coated and hydrophilic, non-waxy parts [21]. Superhydrophilic surfaces of Bromeliaceae (flowering plants) are utilized for absorbing water and nutrients [20]. Superhydrophilic surfaces have been also studied for anti-fogging effect [22, 23]. Superhydrophobic and superhydrophilic properties of the fabricated surface will be discussed.

1.2 Applications of Anti-reflective and Superhydrophobic/philic Surface

Multifunctionality from bio-inspired surfaces, discussed above, can be used for a wide range of applications including omnidirectionally broadband anti-reflective surface for solar cell panel, as well as anti-fogging optical lens for microscope operating in humid biological environment. Figure 1-5 represents a schematic of the fabricated anti-reflective and superhydrophobic/philic surface, which obtain subwavelength periodic high aspect ratio nanocone structures on both sides.

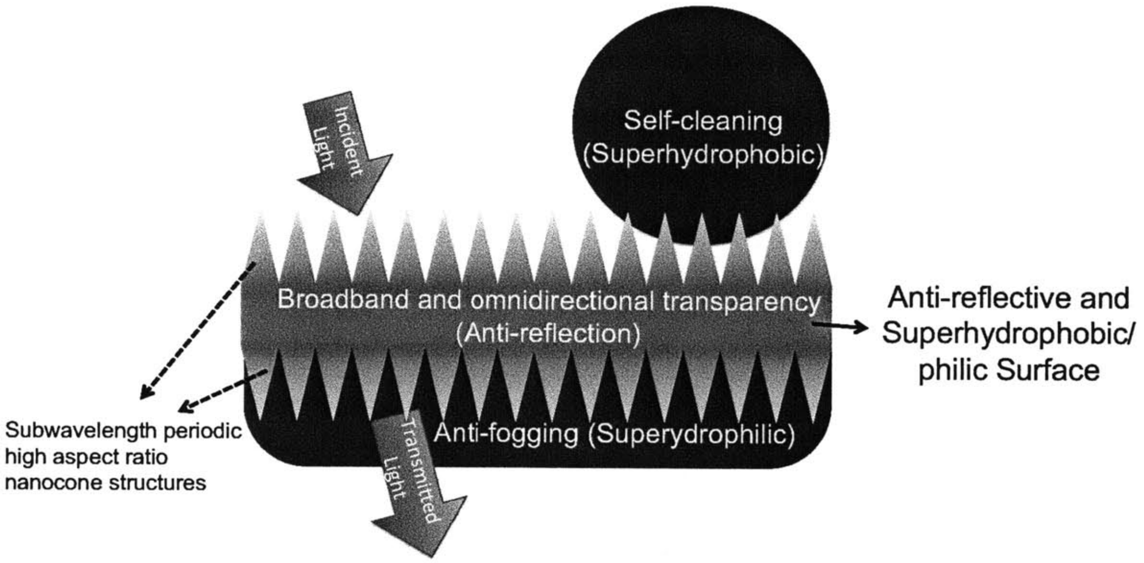

Figure 1-5: Schematic of the anti-reflective and superhydrophobic/philic surface

Windows with the nanostructures on its both surfaces can enhance transmission, and at the same time make the surfaces selectively superhydrophobic and superhydrophilic, such as self-cleaning (outside) and anti-fogging (inside) glass.

This anti-reflective and superhydrophobic/philic surface can also be used for any optical protective elements. In this case of optical elements in digital cameras or commercial lithography equipments, almost 99% of the incident light with wide angle can be collected without any loss. Using such non-reflective protective glass will also eliminate interference effects typically observed for regular glass. Due to the unique wetting properties, dusts and particles on the surface can be easily removed with water. This application is useful for solar cell, since the efficiency of solar cell can be degraded by dust contamination and Fresnel reflection losses. In the case of humid condition, it can be used for anti-fogging glass, and good images may be taken without any bubbles on the lens. If we extend this design approach, we can invent a self-cleaning anti-reflection radar or anti-fogging stealth window for aircrafts in the sense that natural multifunctionality stems from the purpose of camouflage.

1.3 Dielectric Aperiodic Nanostructured Luneburg Lens in Optical Frequencies

Nanostructures are used to acquire a distribution of effective index of refraction by effective medium theory, when those are sufficiently smaller than the wavelength of light. Moreover, the spatial distribution of refractive index, which is called gradient index (GRIN), has an ability to bend light passing through its gradient index region. In this work, the fabrication of an aperiodic nanostructured lens, which converges parallel rays on a point located on the opposite edge of the lens with the nanostructures whose sizes are smaller than wavelength, will be covered.

1.4 Outline of thesis

In this thesis I present the fabrication of subwavelength periodic high aspect ratio nanocone structures and its performance. All the fabrication processes are presented in Chapter 2. Lloyd's mirror system is used for recording the first periodic patterns on resist layer. High aspect raio nanocone structures directly on a fused silica wafer through a novel method, which is a multiple shrinking mask method and reactive ion etchings, could be achieved. The experimental and testing results are summarized in Chapter 3. Transmission measurements are used to evaluate the success of fabrications and prove anti-reflective performance. Beneficial properties of the fabricated nanotextured surfaces such as a robust self-cleaning effect derived from superhydrophobicity or an enhanced anti-fogging property resulting from structural superhydrophilicity will be quantified and examined. Chapter 4 covers fabrication of the dielectric aperiodic nanostructured Luneburg lens.

Chapter 2

Fabrication of Subwavelength Periodic High Aspect Ratio Nanocone Structures

2.1 Introduction

Nanostructured surfaces have been widely studied for their superior optical and wetting properties such as antireflection and superhydrophobicity/hydrophilicity [24, 25, 26]. Due to the subwavelength feature size, the nanostructures behave as an effective medium with gradually varying index of refraction. Such a surface can be used to suppress Fresnel reflection at material interfaces, acting as an antireflection surface and allowing broadband light to pass through without reflection losses [27]. In addition, both hierarchical roughness from those structures and intrinsic chemical property of the surfaces can induce artificial superhydrophobicity and/or superhyrdrophilicity, which can be applied as self-cleaning and anti-fogging surfaces, respectively [28, 29].

Although these notable performances of multifunctional surfaces are well understood, fabricating defect-free nanostructured surfaces with multiple functionality remains a difficult engineering challenge due to limitation of existing nanofabrication methods. The performance of these nanostructured surfaces are determined by their geometry, it is critical to fabricate gradually tapered structures with small feature sizes (Λ) and large height (H). The higher aspect ratio (H/Λ) the structures have, the better optical and wetting properties they exhibit [30, 31].

As mentioned in Chapter 1, nanostructured surfaces can be prepared by several existing fabrication methods, such as electron beam lithography [15], nanoimprint-/polymer replication [16], deposition of multilayer porous films or chemical materials [13], and colloidal lithography [17, 18]. However, it is difficult to achieve high aspect ratio structures (>5) with a gradual tapered profile on large-area ($\backsim cm^2$) using these techniques. In other words, the properties of subwavelength nanocone structures fabricated using existing techniques have limited performance.

I used a novel method of using multiple shrinking mask etching to fabricate periodic high aspect ratio nanocone structures with interference lithography, which has the ability to create large-area ($\backsim cm^2$) periodic nanostructures with a low-cost and simply tool [32]. The structure aspect-ratio fabricated using this method can be precisely controlled and have been demonstrated as high as 6. In this chapter, the fabrication of subwavelength periodic high aspect ratio nanocone structures and the fabrication result will be described.

2.2 Interference Lithography

The principle of interference lithography is that two spatially and temporally coherent beams intersect and form a standing wave pattern in a region where they overlap. This sinusoidal standing intensity pattern is recorded on a positive or negative resist, and then desired grating is achieved, as shown in Figure 2-1. The intensity pattern [33] is then given by

$$I = |\vec{E}_L + \vec{E}_R|^2 \tag{2.1}$$

where $\vec{E}_L$ and $\vec{E}_R$ are the electric fields of the left and right incident beams, respectively. The fields become

$$\vec{E}_L = \hat{e}_L A_L \exp\left(-j\omega t - nkx\sin\theta + nky\cos\theta\right) \tag{2.2}$$

$$\vec{E}_R = \hat{e}_R A_R \exp\left(-j\omega t + nkx\sin\theta + nky\cos\theta\right) \tag{2.3}$$

where $\hat{e}_L$ and $\hat{e}_R$ are unit vectors indicating the polarization, and A_L and A_R are the amplitudes of the left and right beams, respectively, $k = \frac{2\pi}{\lambda}$ is the wave vector, $w = 2\pi f$ is the frequency, and n is the refractive index of the medium. The intensity profile along the x-direction is

$$I(x) = A_L^2 + A_R^2 + 2A_L A_R(\hat{e}_L \cdot \hat{e}_R)cos(2nkx\sin\theta) \tag{2.4}$$

The period Λ of the intensity pattern becomes

$$\Lambda = \frac{\lambda}{2n\sin\theta} \tag{2.5}$$

For recording a standing wave pattern on a positive resist, I used Lloyd's mirror system [34], which is shown in Figure 2-2. In the Lloyd's mirror, the mirror divides wavefronts from one coherent laser source into two overlapping beams, and those two beams generate the interference pattern. The source is a 50 mW HeCd laser with a 300 mm coherence length. The laser is spatially filtered using a lens and a pin- hole

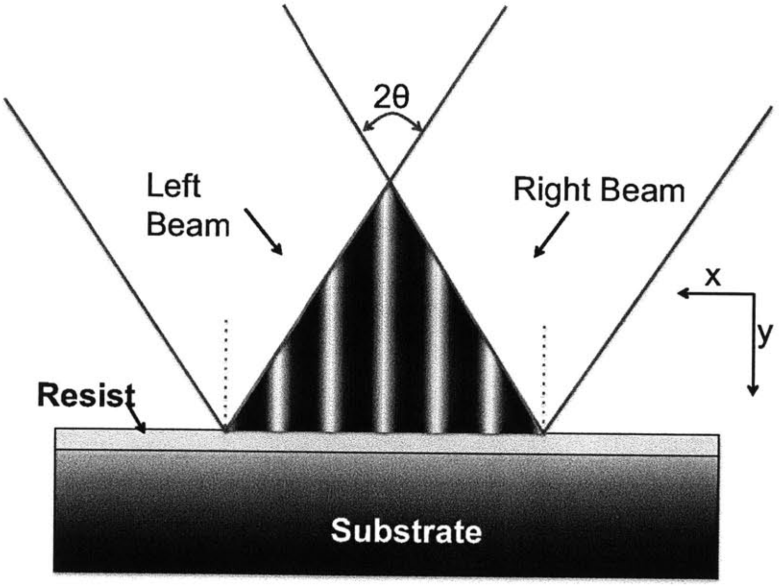

Figure 2-1: Concept of interference lithography

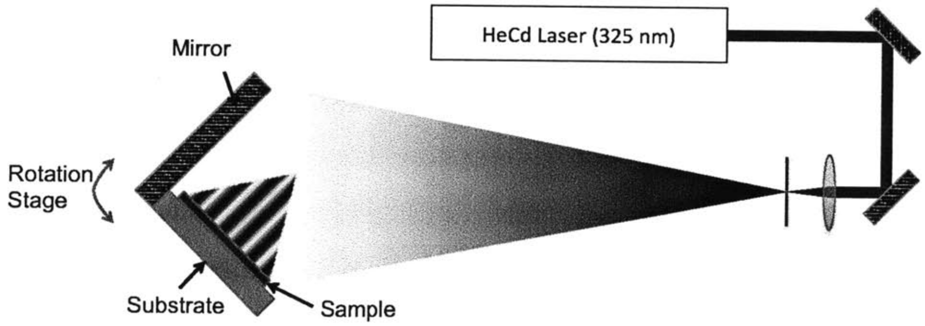

Figure 2-2: Schematic of Lloyd's mirror system

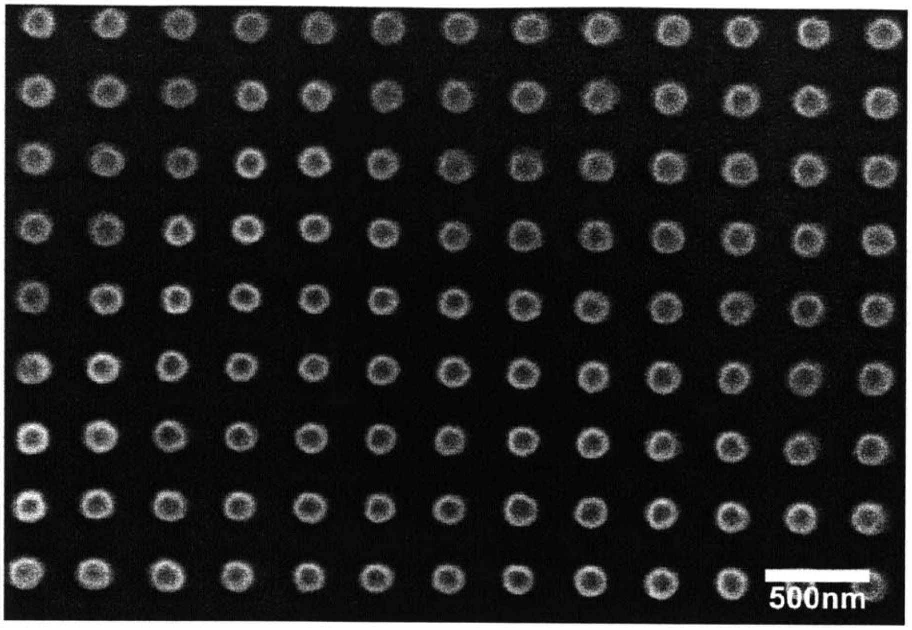

Figure 2-3: PFi-88 photoresist dot array patterned by double exposures at 90° to each other with interference lithography

with a nominal diameter of 5 μm [35]. The patten I used for fabricating periodic high aspect ratio nanocone structures was written on a PFi-88A2 positive resist layer with double exposures at 90° to each other. An anti-reflective coating (I-con 7) was used on all the samples. Figure 2-3 shows the successfully developed dot array patterns from the top. The period is 200 nm.

2.3 Multiple Shrinking Mask Method

The conventional approach of fabricating tapered nanocone structures is based on a single hardmask, as represented in Figure 2-4. The numbered arrows in Figure 2-4 denote etching processes. Both thickness of the hardmask (t_1) and etch selectivity between the hardmask and the substrate would determine the height of the structures. However, this process is limited to the etch rate and thickness of the single hardmask. In other words, the final height is restricted to the material of the hardmask and its thickness, so that the height and profile of the nanocone structures might not be effectively controlled.

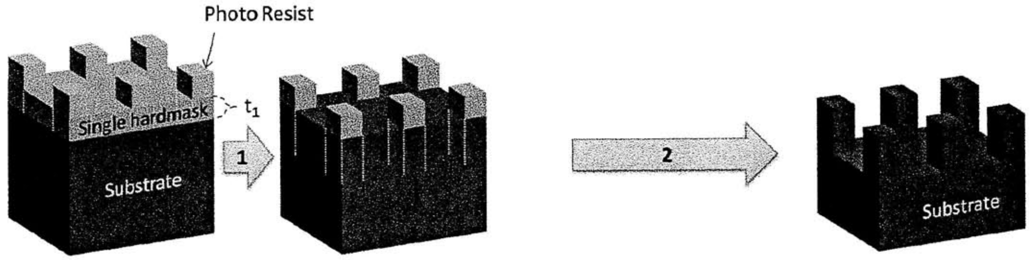

Figure 2-4: Schematic of conventional hardmask etching process

The proposed idea is based on using multiple-step plasma etching using shrinking masks to get more flexible choices of materials and thicknesses for better control of the height and profile of nanocone structures. Figure 2-5 shows a schematic of the proposed fabrication process. The numbered arrows indicate the number of etching processes, and can be extended to as many as desired (2 etch cycles are depicted in the diagram). Since the process is based on standard CMOS plasma etching, it is compatible and can be adapted with any lithographic techniques. Any desired nanoscale pattern can be transferred to the first mask, which have high etch selectivity to the pattern during the first etching. The patterned mask (the first mask) is then used as another protective layer to etch through the second etch mask. To end with the patterned second one, the desired nanostructures are appeared through the final etching. The height of the structures can be designed and determined by etching selectivity between 2 mask layers and their thicknesses (t_1 and t_2).

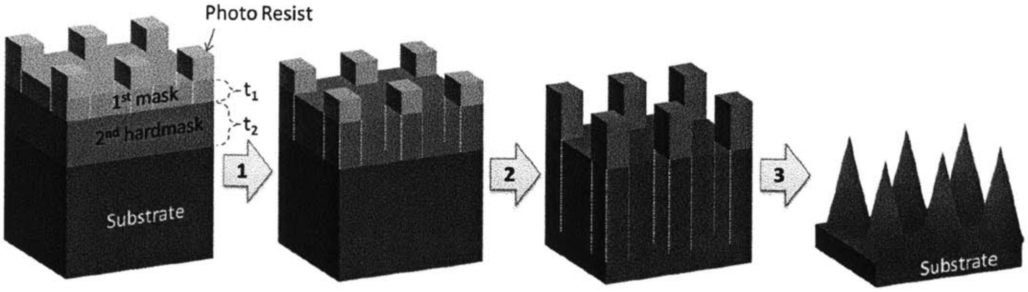

Figure 2-5: Schematic of multiple shrinking mask etching process

The key feature is utilizing mask materials that are etched, but at a much slower rate. This allows the resulting profile to be tapered. Figure 2-6 illustrates the schematic cross sections of the last etching process, which is equivalent to the arrow 3 shown in Figure 2-5, for tapered nanocone structures. An anticipated aspect ratio of nanocone structures results from not only the dimension of the width of the first beginning pattern (w_2) but also the thickness of the second mask (t_2). The underlying mask being etched away tends to be directional, at the same time the second mask is shrinking. It covers the tip of the nanocone structures for providing a desired slope of nanocone structures, which is the aspect ratio (H/Λ) in order words, until the moment that it is fully removed. If higher H is desirable, the etch process can be repeated by using the tapered profile to etch into another material. Note that since all of the processes are done in vacuum, structure collapse associated with surface tension in wet etches are avoided. In the next section, the whole fabrication processes will be explained in detail.

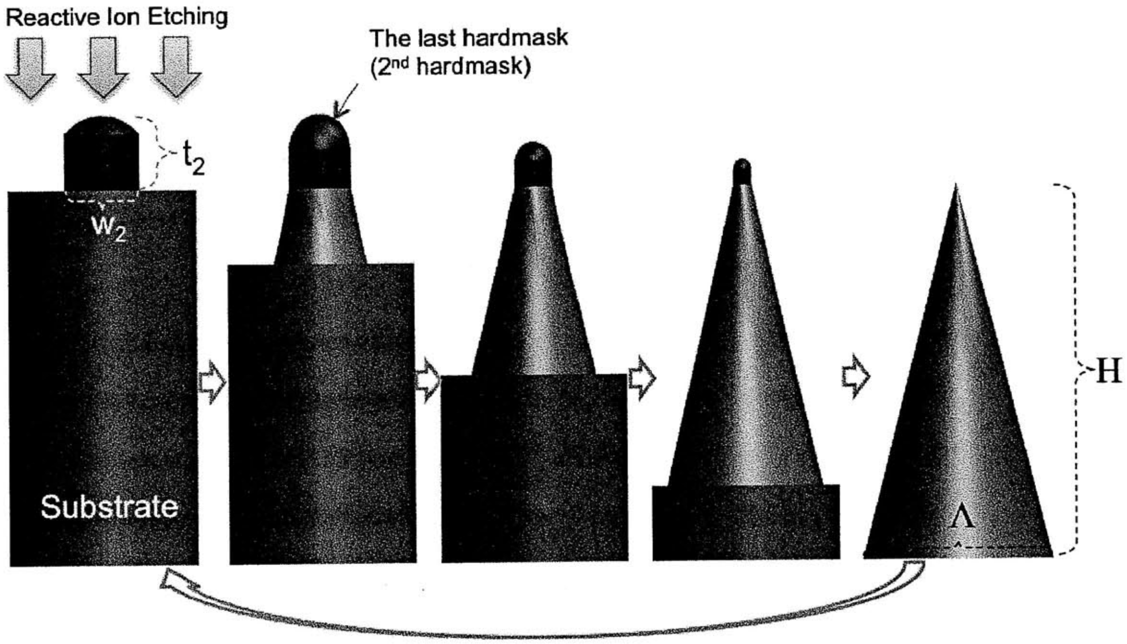

Figure 2-6: Process of fabricating high aspect ratio nanocone strucures

2.4 Fabrication Process

The nanostructure fabrication steps are described as follows, and are also shown in Figure 2-7. All the thicknesses of multiple layers were optimized for interference lithography. 240nm-thick polysilicon films were deposited on both sides of a 6 inch UV graded fused silica wafer with chemical vapor deposition technique as the second hardmasks for getting a high aspect-ratio SiO_2 structures. 4-μm-thick photoresist (S1813, Shipley) were spun on both sides of polysilicon layers of the fused silica wafer as protective layers, and the wafer was cut into 4 pieces of 45mm by 45mm samples. The photoresist on top of polysilicon was cleaned with NMP (Positive resist striper, BASF) and RCA cleaning [36] for 20 minutes, and was sonicated for 5 minutes at room temperature. 340nm-thick-hydrogen silsequioxane (HSQ14, Dowcorning) films were then spun on both sides of the sample and hard-baked at 500°C in the oven for 11 hours to be cured as the first hardmask, because cured HSQ layer is similar to SiO_2 etch mask layer [37].

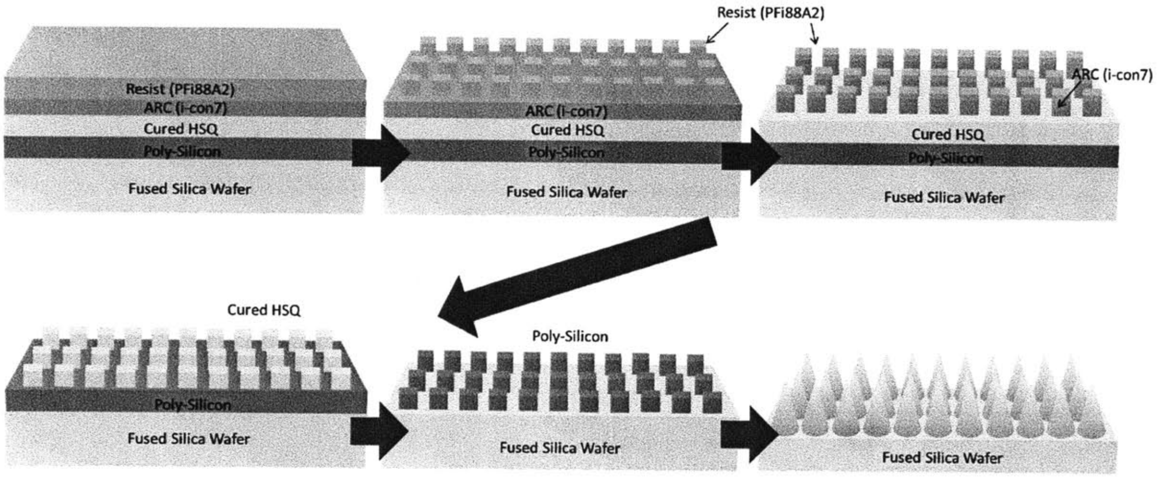

Figure 2-7: Schematic illustration of the fabrication process for high aspect ratio nanocone structures directly on top of a fused silica wafer

After RCA cleaning, sonification, and plasma oxygen etching for 30 seconds in order to remove organic junks and particles, 105nm-thick-ARC (I-con 7, Brewer Science) were spun on both side and baked at 180°C in the oven for 1 hour. For baking, the oven was used instead of hot plate, because both sides of the sample should be protected.

Anti-reflective coatings are commonly utilized during photolithography process in order to improve the photoresist profile (or contrast) and reduce the line width variation caused by scattering and reflecting light. Since a thickness of anti-reflective coating (ARC) layer is one of the most critical factors in interference lithography, the optimized thickness of ARC layer (I-con 7) was calculated from multilayer Fresnel reflection and transmission calculation [38]. In these multi-stacked layers, 102.3 nm of ARC layer can minimize the reflecting light on the interface between ARC layer and cured HSQ layer, as shown in Figure 2-8. Based on experiment results, the reflection must be less than 1% to reduce a possibility on fabricating low duty cycle resist posts.

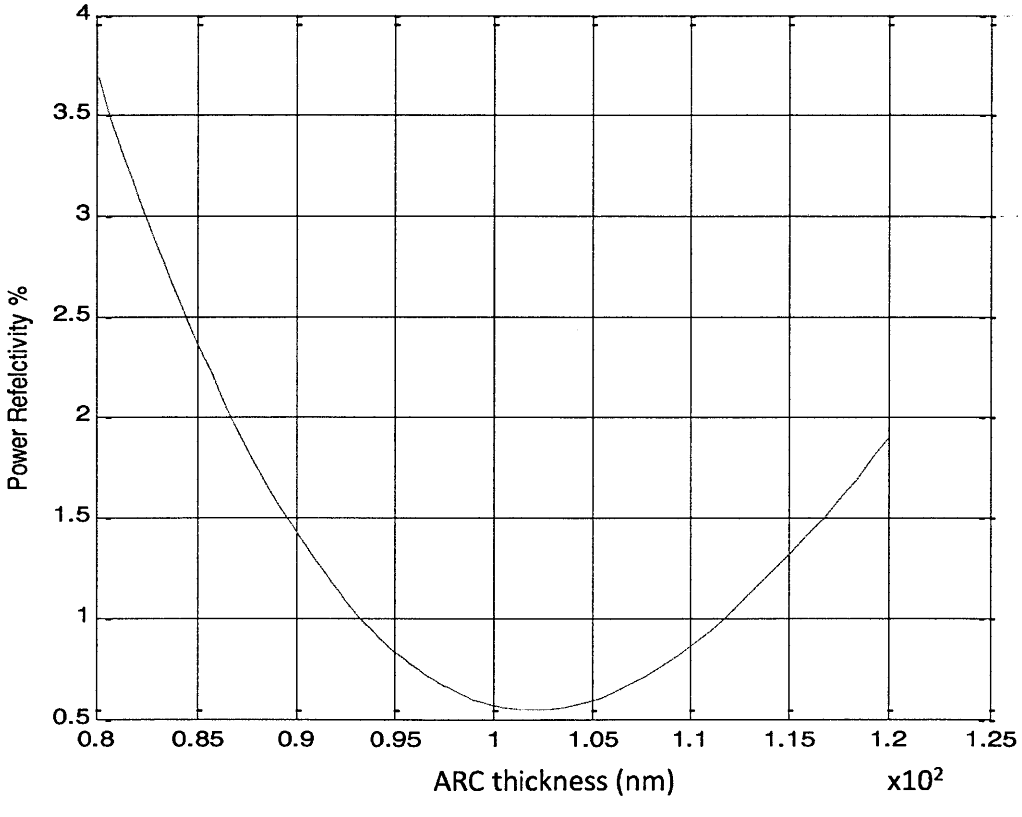

Figure 2-8: Calculated reflection on the interface between ARC and cured HSQ layer in Lloyd's mirror system with prepared multilayer

A 200nm-thick-positive photoresist (PFi-88A2, Sumitomo) was spun on only one side of the sample, while 4-m-thick photoresist (S1813, Shipley) was spun on top of the backside of the sample as a protective layer. Then, it was baked on the hot plate at 180°C for 90 seconds.

With Lloyd's mirror, a 325 nm wavelength laser beam makes interference pattern with a 200 nm period standing wave onto the photoresist. The two exposures are carried out at 90° to each other, and exposed photoresist is developed to leave a pattern of posts.

Duty cycle of the pattern varies with respect to exposure doses, as shown in Figure 2-9. An inset indicates the result of linear fitting. This is useful for estimating the duty cycle. Figure 2-10 also shows cross-section SEM micrographs of dot pattern with different exposure doses, which are controlled by exposure time and intensity of the source in Lloyd's mirror system . As expected, the more dose are exposed on the resist, the less duty cycle is achieved.

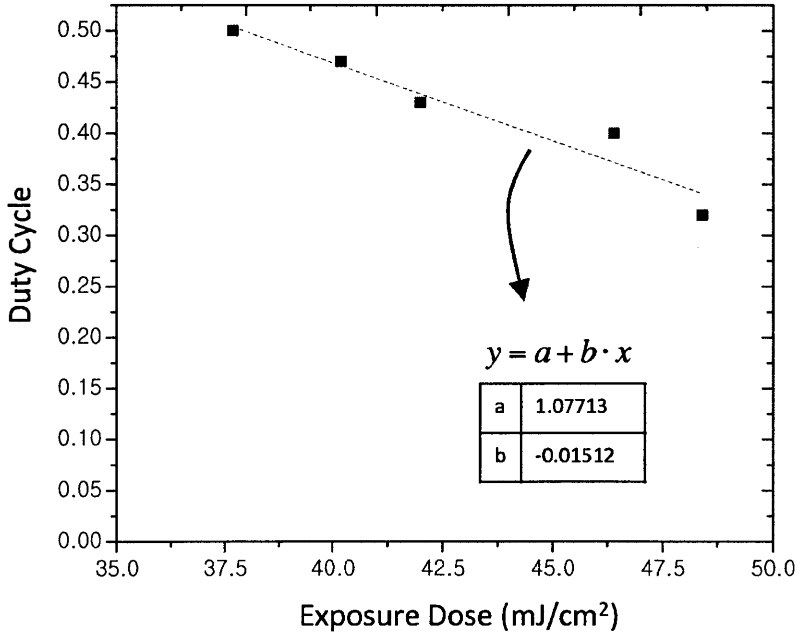

Figure 2-9: Duty cycle of the patterns with respect to different exposure doses

Controlling duty cycle of the pattern is critical for the success of patterning dot

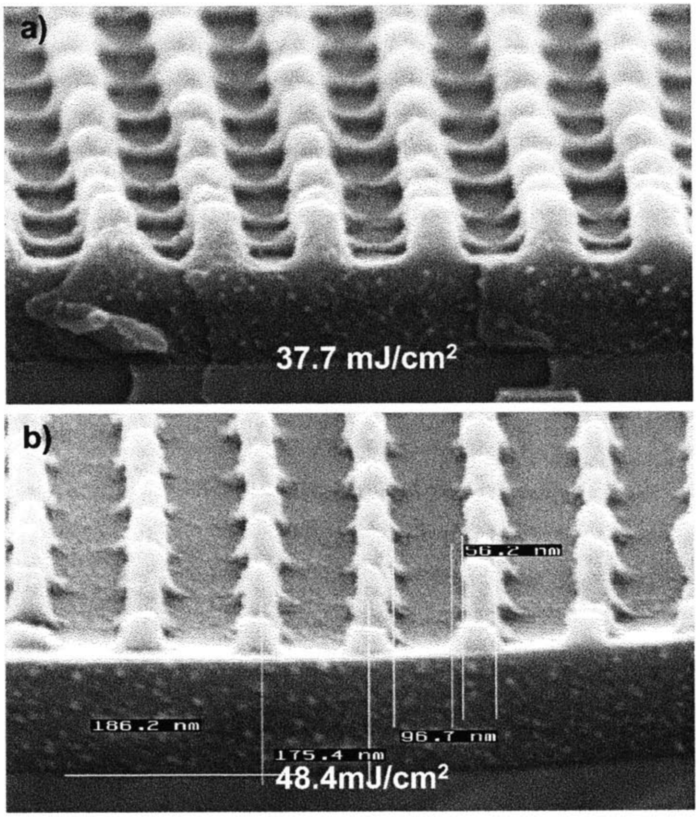

Figure 2-10: Cross-section SEM micrographs of two duty cycles with respect to exposure doses (37.7mJ/cm^2, 48.4mJ/cm^2) with 325 nm laser

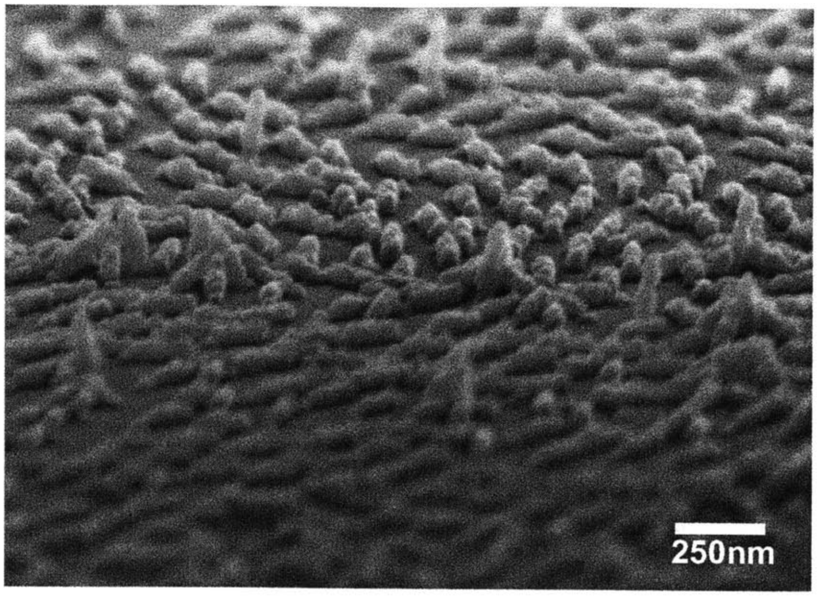

Figure 2-11: SEM micrograph of collapsed PFi-88 posts (Duty cycle: 0.27)

array, since PFi-88 resist posts collapse each other in Figure 2-11 when the duty cycle is less than 0.3. Surface tension generates shear stress directly on the posts and makes them breakdown to the surface during drying process after development, since posts with low duty cycle of the pattern has low yield strength. Further research is needed to find critical height of the resist and duty cycle of the pattern. To do that, Young's modulus of unexposed PFi-88 is required. To avoid this collapses, 0.4~0.5 duty cycle was used for the fabrication of nanostructured surface.

The ARC layer is etched by O_2 reactive ion etching (RIE) to make the same array of posts as the developed resist. The pattern was transferred into cured HSQ layer using CHF_3 reactive ion etching for 13 minutes as shown in Figure 2-12. An oxygen and CF_4 reactive ion etching processes were used to remove the residual photoresist and open the polysilicon surface from cured HSQ, for 2 minutes and 10 seconds, respectively. Due to the cured HSQ pattern (similar to SiO_2), the pattern was faultlessly transferred to 240nm-thick polysilicon layer with HBr reative ion etching for 6 minutes, which was considered and calculated with etch rates between the hardmask and fused silica in order to get the high aspect ratio. Figure 2-13 depicts a cross-section SEM micrograph of the sample after HBr etching. Finally, the high aspect

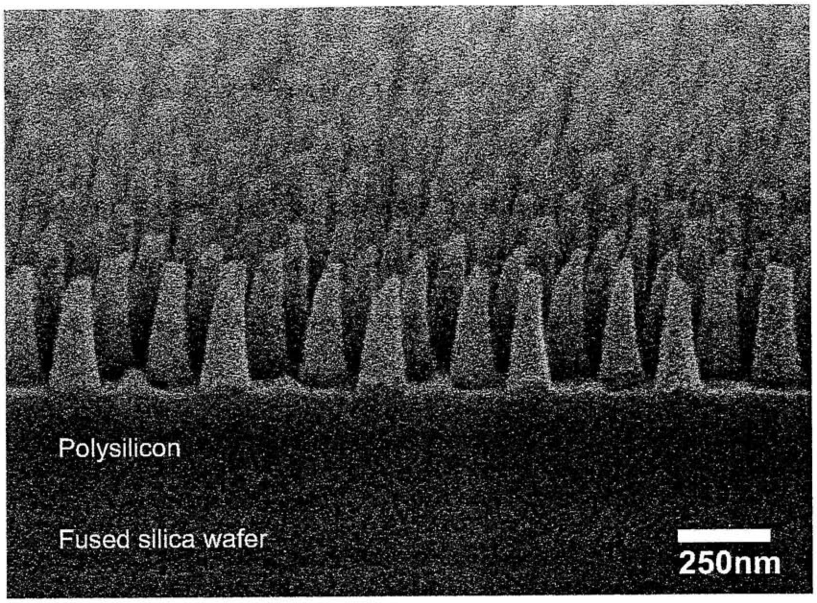

Figure 2-12: Cross-section SEM micrograph of the sample after the first CHF_3 reactive ion etching

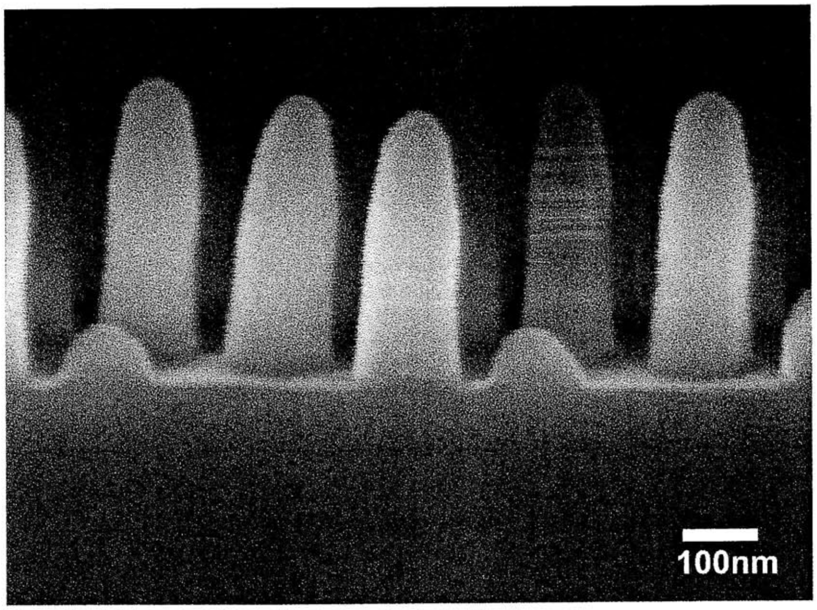

Figure 2-13: Cross-section SEM micrograph of the sample after HBr reactive ion etching

ratio nanocone structures were successfully fabricated due to polysilicon hardmask patterns with CHF_3 reactive ion etching for 40 minutes, as depicted in Figure 2-6.

To get a better optical performance, a piece of the fused silica is needed to be patterned on both sides. Additional repeatable processes were conducted as described below. After 40 minutes of RCA cleaning, a 4μm-thick-resist (S1813) was spun onto the patterned surface being shielded. ARC layer and positive photoresist (PFi-88) were spun onto the backside of the sample, consecutively. A pattern of photoresist posts was fabricated with double exposures and development, and it was transferred down to fused silica with the same fabrication steps and conditions that were mentioned above. After RCA cleaning, the rest of polysilicon was removed by TMAH etching without attacking the fabricated fused silica nanostructures on both sides. For TMAH etching (25%), the etch rate of silicon is 400nm/min at 80°C and the etch rate of silicon oxide is 0.9Å/min at 80°C [39]. The rest of polysilicon on top of sample was etched by TMAH etching (25%) at 80°C for 1 minute, and then cleaned with water.

In order to get high aspect-ratio nanostructures, two hardmasks are utilized as described in the previous section. Desired pattern is transferred to the first hardmask, which have high etch selectivity during reactive ion etching. The patterned first hardmask is then used for another hardmask to etch through the second hardmask. To end with the patterned second hardmask, the desired nanostructures are appeared through the final reactive ion etching. The aspect ratio of the structures can be designed and determined by the dry etch selectivity between 2 mask layers and their thicknesses. Through the etch rate tests, the etch depth of SiO_2 in CHF_3 reactive ion etching for 10 minutes is 250 nm, while the etch depth of polysilicon in the same condition is 50 nm. 310nm-think cured HSQ layer and 240nm-thick polysilicon film were used as the first and second hardmask, respectively, so as to get high aspect ratio (5~6) nanocone structures.

All the fabrication process is described in Table A.1.

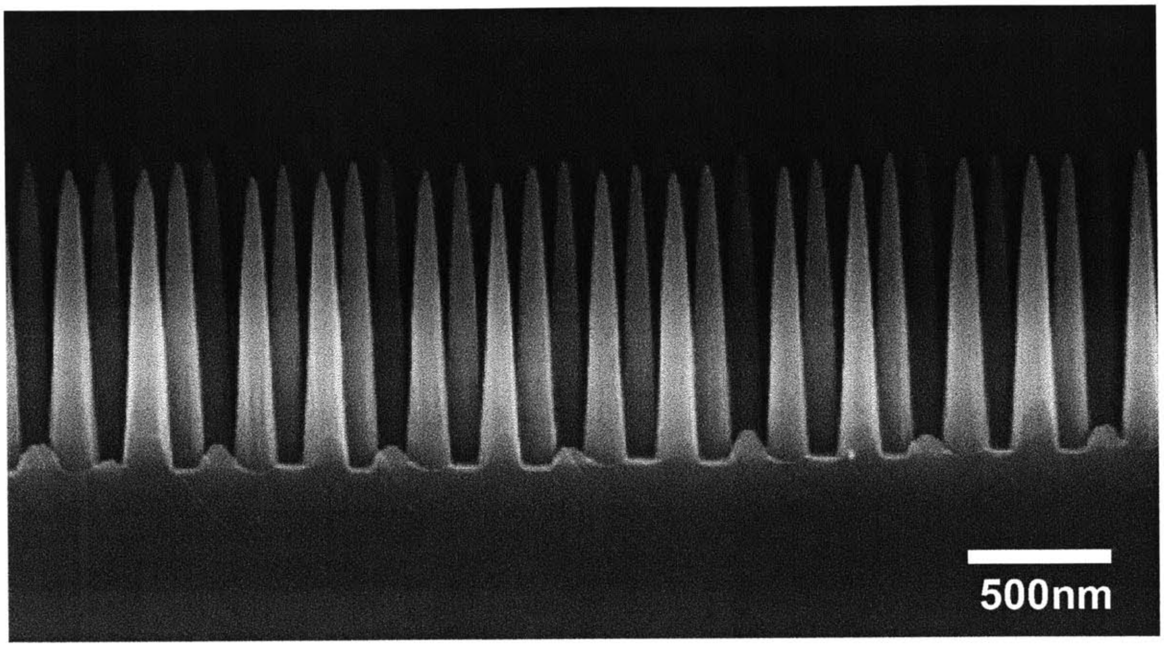

Figure 2-14: Cross-section SEM micrographs of fabricated high aspect ratio subwavelength nanostructures which period is 180 nm

2.5 Fabrication Result

For the development of surfaces possessing nearly lossless transmission, a fused silica was selected as the substrate material, while most of the recent work on subwavelength antireflection structures is based on absorptive materials (e.g., Si, GaAs, carbon nanotubes, etc.) which suppress surface reflection but do not enhance transmission. The high aspect ratio nanostructures was patterned over a large area of the substrate using orthogonal exposure through interference lithography to yield a defect-free periodic square array.

Figure 2-14 depicts a 180 nm-periodic array of tapered nanocone structures that are over 1 μm tall with 10-20 nm radius of curvature at the tip directly on a fused silica substrate. A novel multiple shrinking mask etching was developed to achieve such a high aspect ratio nanocone structures. A 200nm-periodic array of nanocone structures was also fabricated, as shown in Figure 2-15. Its optical and wetting properties will be discussed in Chapter 3.

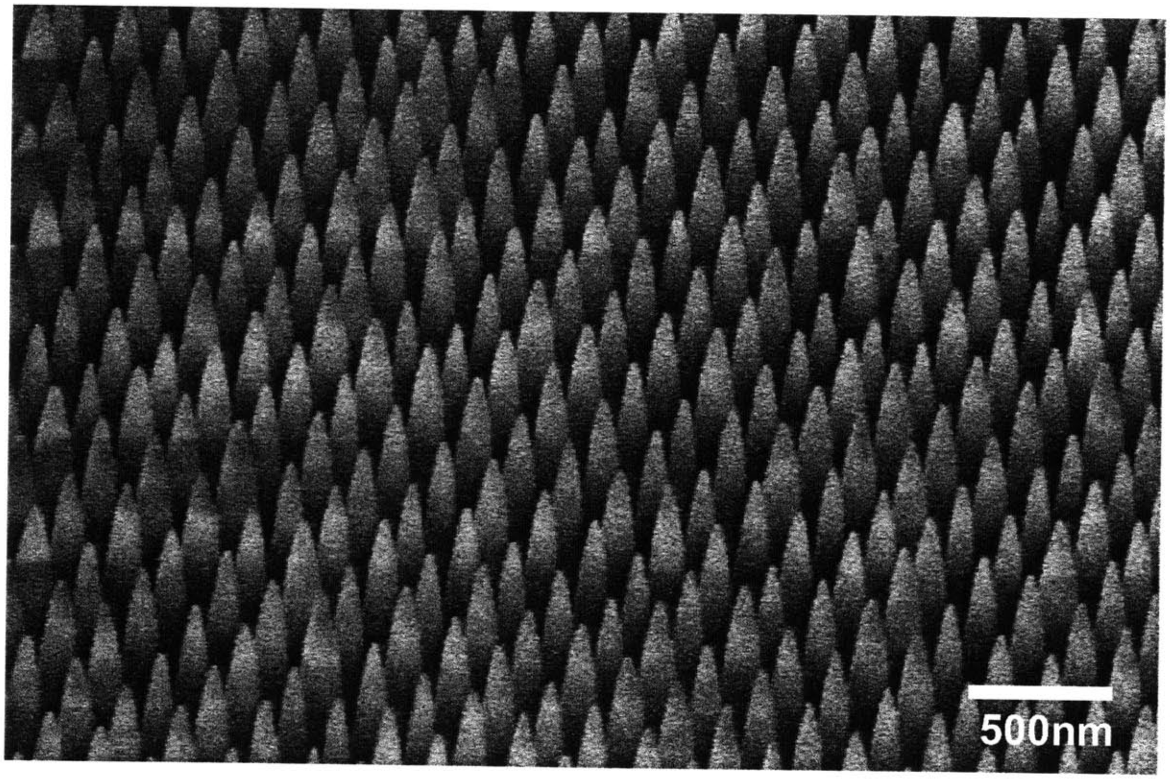

Figure 2-15: Cross-section SEM micrographs of fabricated high aspect ratio subwavelength nanostructures which period is 200 nm

Chapter 3

Testing and Characterization of Subwavelength Periodic High Aspect Ratio Nanocone Structures

3.1 Introduction

Subwavelength periodic high aspect ratio nanocone structures directly created on a fused silica wafer lead to superior optics and wetting performances. In order to prove optical properties on subwavelength periodic high aspect ratio nanocone structures, transmission measurements with respect to incident angle (0° to 80°) of polarized lasers (543nm and 633nm) and broadband wavelength (185nm to 1750nm) at normal incident angle were conducted. For the experiments, single-side and double-side patterned samples are prepared. All the theoretical data were modeled using rigorous coupled wave analysis (RCWA) [40, 41, 42]. Contact angles were measured on both silanized nanotextured and untreated surfaces in order to show superhydrophobicity and superhydrophilicity. Water drop impact experiment was also carried out. To show multifunctionality of the fabricated nanotextured surface, optical transmission measurements for the quantification of self-cleaning and anti-fogging properties were conducted.

3.2 Angle Transmission Measurement

The nanocone structures exhibits enhancement of optical transmission. The experiment was conducted in the experimental setup as illustrated in Figure 3-1. Figure 3-2 depicts the measured transmission for a fused silica substrate (theoretical data), and single-side and double-side patterned surfaces. The measurements were carried out over large incident angles from 0° to 80° using both TE- and TM-polarized lasers with 543 nm and 633 nm wavelengths. The theoretical data shown are calculated using RCWA, and agree well to the experimental measurements. Figure 3-2 a) and b) display the measured transmission of TE-polarized light, which is well known for dramatic transmission degradation at large angles. At both wavelengths, the transmission of the double-side patterned surfaces is enhanced to be above 90% for incident angles of up to 75°, while the transmissions of typical glass is around 38% at 75°. The dramatic increase on transmission at large incident angle is due to the high aspect ratio of the fabricated structure, and is not observed in previous work. Note for the single-side patterned sample, the transmission is limited by the Fresnel reflection from the back surface, which has no subwavelength nanocone structures.

Figure 3-2 c) and d) show measured transmission of TM-polarized light, which exhibits the well-known Brewster effect. As shown in the graphs, both percentages of the measured transmission of single and double-side fabricated samples are over 90% at 70°. One interesting observation is that there is no specific Brewster angle associated with the nanocone surface, since it is not a discrete index interface. In-

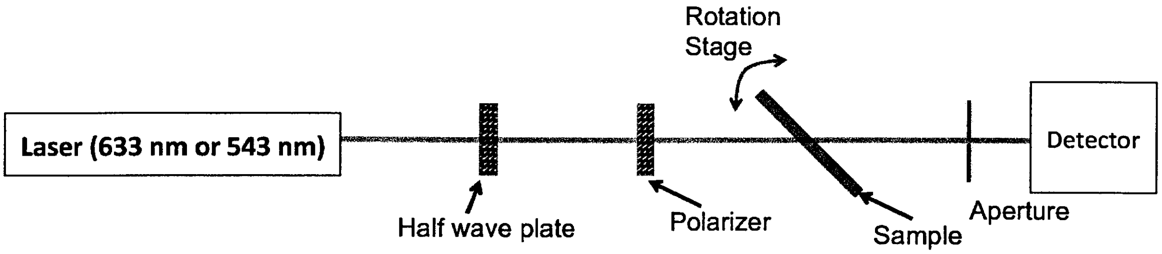

Figure 3-1: Schematic of optical transmission measurement setup with respect to incident angle (top view)

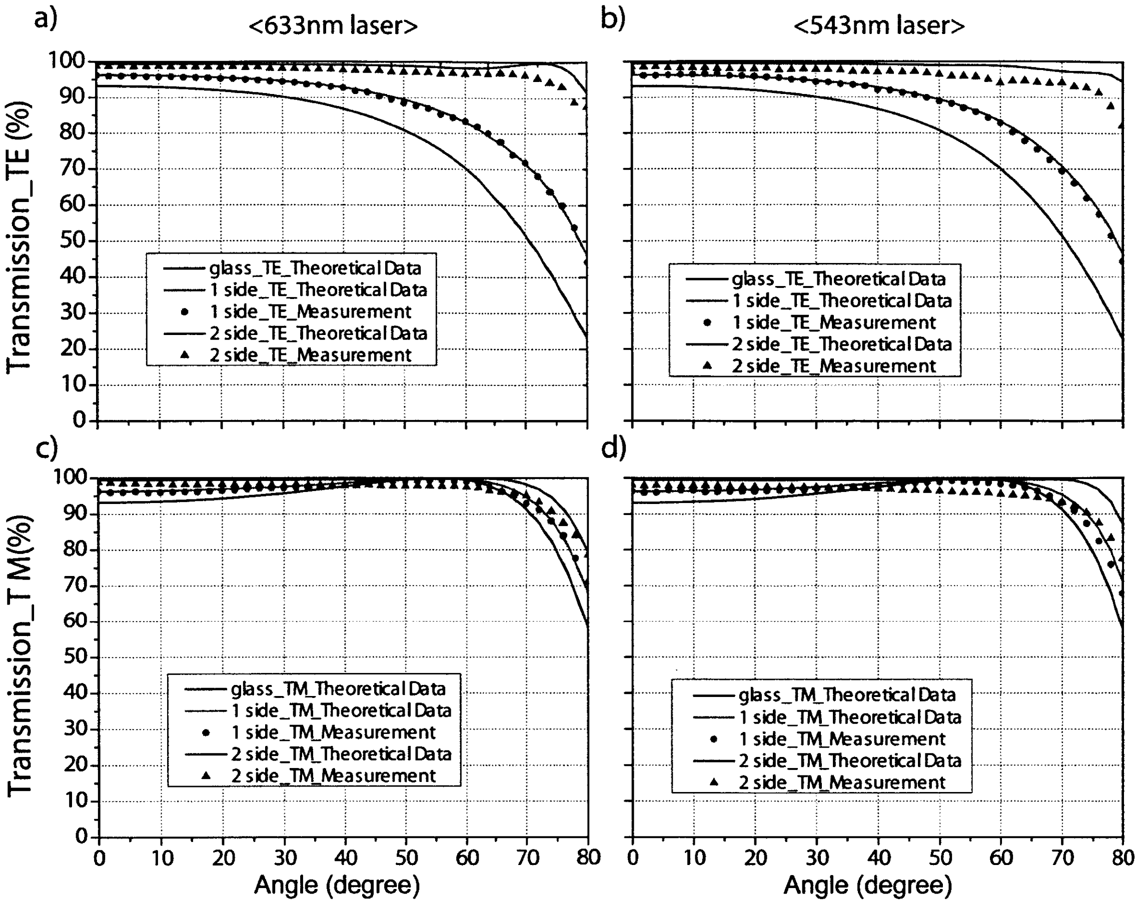

Figure 3-2: Measured transmission of fabricated single and double-side sample using 543 nm and 633 nm wavelength for both TE and TM polarization (a) - (d) as functions of incident angle.

stead the subwavelength structure offers enhanced transmission over a broad range of incident angles. The fabricated double-side sample has slightly lower measured transmission due to defects induced while processing both sides of the substrate. The single-side sample, on the other hand, does exhibit the Brewster effect to the back surface, and the transmission increases to 99.4% at 56°. Again the transmission from the single-side sample is dominated the Fresnel reflection from the back surface. These experiments show enhanced transmission over large incident angles.

3.3 Broadband Transmission Measurement

The transmission measurement was carried out over a broad wavelength range (185-1750 nm) at normal incident angle (0°) to examine the spectra response. Cary 500i UV-Vis-NIR Dual-Beam Spectrophotometer was used for this experiment. The transmission of single-side patterned sample matches well with the theoretical model, and is limited by the Fresnel reflection from the unpatterned back surface. The double-side sample exhibits higher than 99% transmission for wavelengths in the range of 770 to 1750 nm, except at 1390 nm, which is caused by the absorbance characteristic of UV-grade fused silica. The measurement shows a drop of transmission at the shorter wavelength bound around 300 nm, which is predicted as the nanocone structures become diffractive. This experiment demonstrates enhanced transmission over a broadband wavelength.

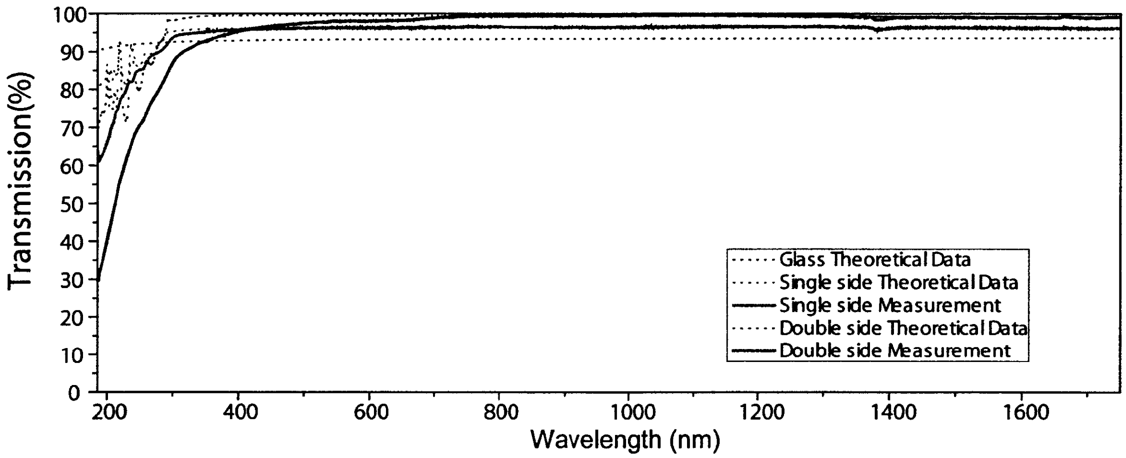

Figure 3-3: Measure broadband transmission for unpolarized light at normal incident (0°)

3.4 Wetting Properties

To modify the wetting property of the nanostructured surface into hydrophobic, the following silane treatment was carried out by a chemical vapor deposition process of 1H,1H,2H,2H-perfluorodecyltrichlorosilane. Samples were placed in an oven together with a few droplets of silane and heated at 90°C for more than 5 hours.

On an untreated flat fused silica surface, water contact angle is around 30 ± 1° whereas silanization increases the equilibrium contact angle up to around 120 ± 1°. High aspect ratio (or high Wenzel roughness [43]) nanotexture promotes the hydrophilicity/hydrophobicity of the flat surface. The apparent contact angle of the nanostructured surface without silane treatment is less than 5°, which is called superhydrophilic. On the other hand, the silanized nanotextured surface shows extremely high apparent contact angle of 163 ± 3°, displaying superhydrophobicity. In Figure 3-4, the fabricated superhydrophobic and transparent anti-reflective surface enables a water droplet that dyed blue to form a spherical bead.

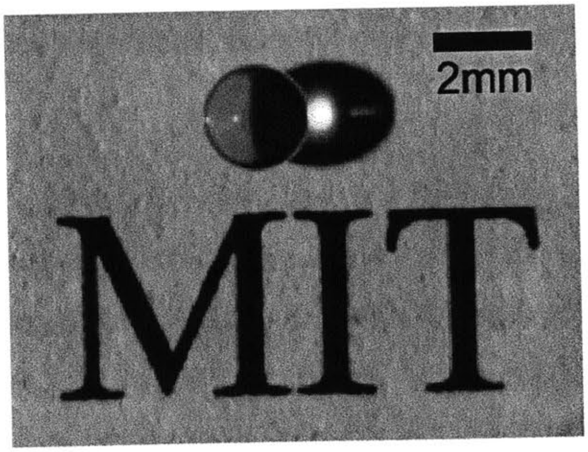

Figure 3-4: Blue-dyed water droplets on the single-side patterned surface on top of printed black letters (1200 X 1200 dpi). The intense reflection of light next to the droplet originates from the focusing by the droplet as a spherical lens.

Enhanced robustness of the Cassie-Baxter state [3] was examined by using water drop impact experiments. Fragmentation and complete rebound (without any residual droplets impaled into the surface texture) of droplets released at the impact

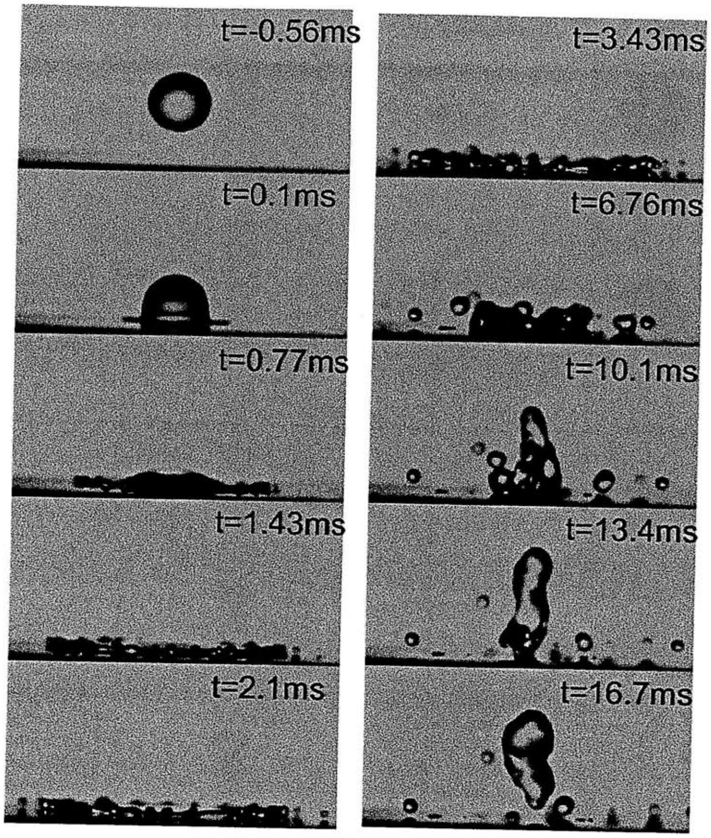

Figure 3-5: Sequential images of water drop impact experiment (Impact velocity = 2.3m/s, Drop diameter = 2.45mm)

height of several meters shows the robustness preventing loss of superhydrophobicity. Figure 3-5 demonstrates sequential images of water drop impact experiment clearly shows the effect of self-stabilization effect and complete rebound at a impact velocity at 2.3m/s.

In addition, the apparent contact angle of the nanostructured surface without silane treatment is less than 5 degree. The contact angle of the fused silica surface without silane treatment is 30°. It is proven that the nanostructured surface itself is superhydrophilic.

3.5 Multifuctionality of the Nanostructured Surface

The abovementioned wetting properties of the nanocone surfaces can be utilized to produce other merits - enhanced transparency on the nanotextured surfaces. In most environments, surfaces are exposed to contaminant opaque particles and light scatters due to fogging, which typically reduce transmission; thus it is important to easily clean a contaminated surface and avoid fogging on a surface for practical applications including windshields and goggles. To quantify the self-cleaning effect and anti-fogging property, the transmission measurements for the fabricated surface and a glass slide surface were carried out using 633 nm red laser. Figure 3-6 shows a schematic of the experimental setup for self-cleaning effect. Figure 3-7 and 3-8 demonstrate that most of three different contaminant particles on the nanotextured surfaces can be removed by at most five droplet impacts (self-cleaning effect derived from highly robust superhydrophobicity), whereas water droplets hardly typical flat glass surfaces because it spreads on the surfaces, distributing the particles on a wider area.

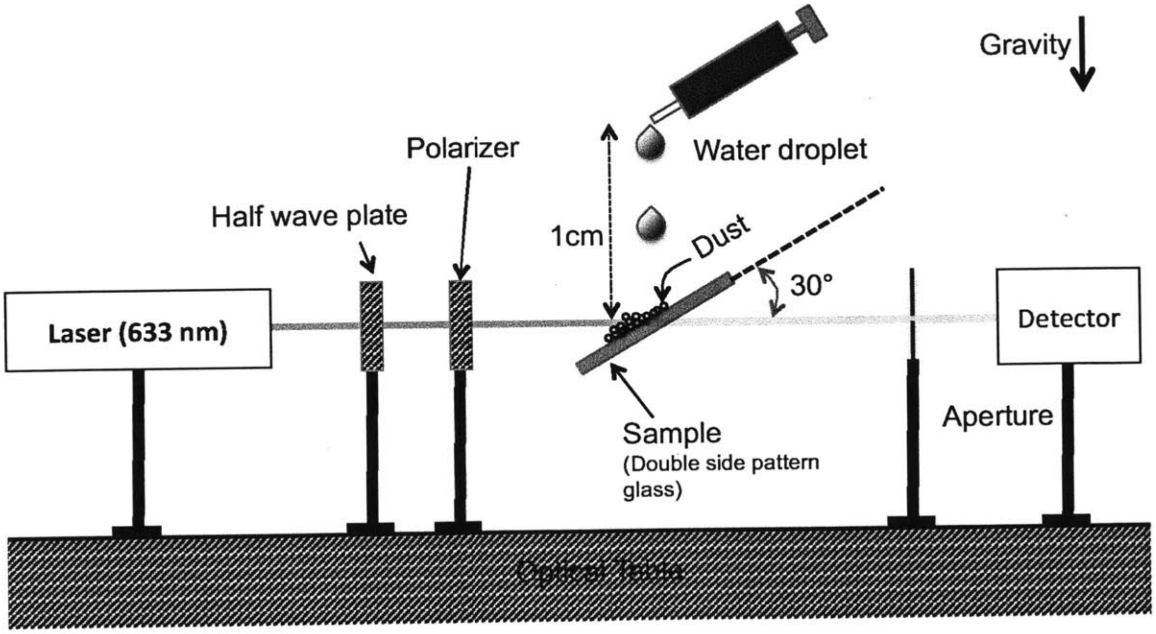

Figure 3-6: Schematic of the experimental setup for self-cleaning effect (side view)

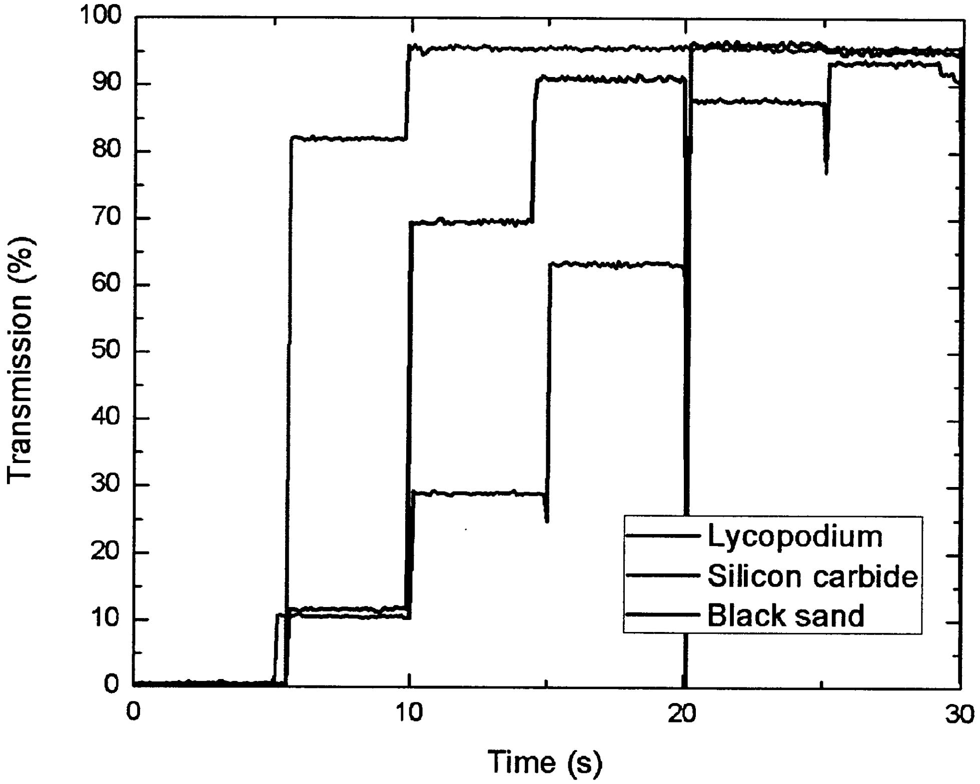

Figure 3-7: Transmission measurements with 633nm red laser with respect to time while water droplets were released at the height of 1*cm* from the inclined surfaces (30°) every 5 seconds on the silanized nanocone surface covered with various contaminant particles

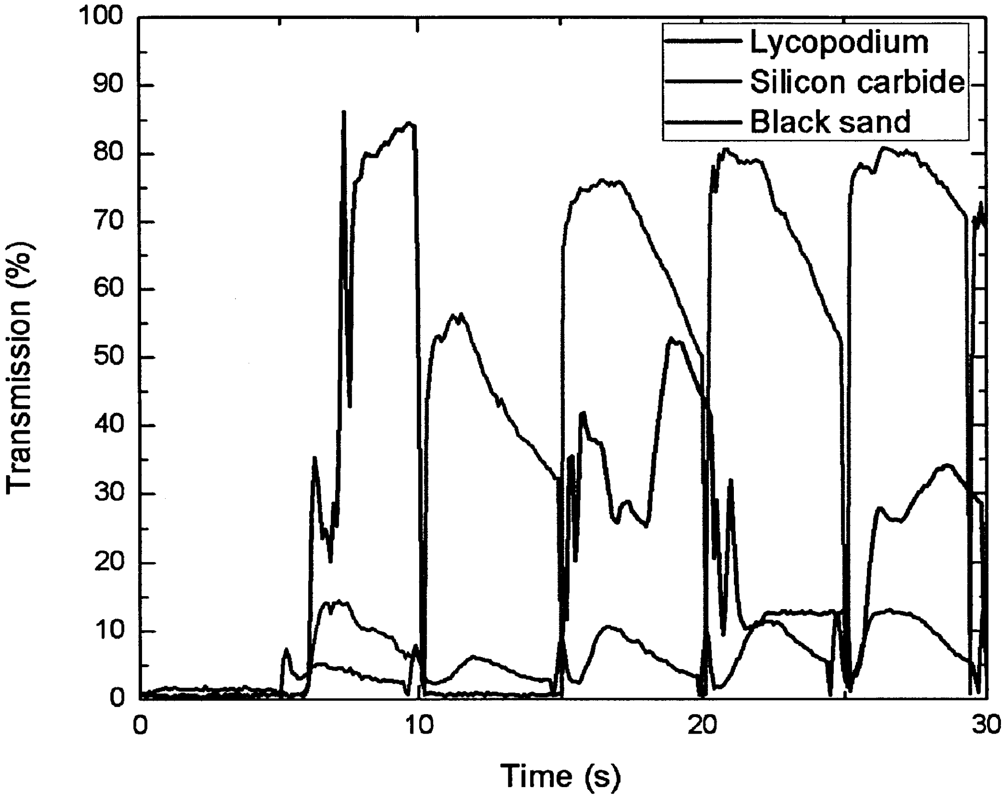

Figure 3-8: Transmission measurements with 633nm red laser with respect to time while water droplets were released at the height of 1cm from the inclined surfaces (30°) every 5 seconds on the glass covered with various contaminant particles

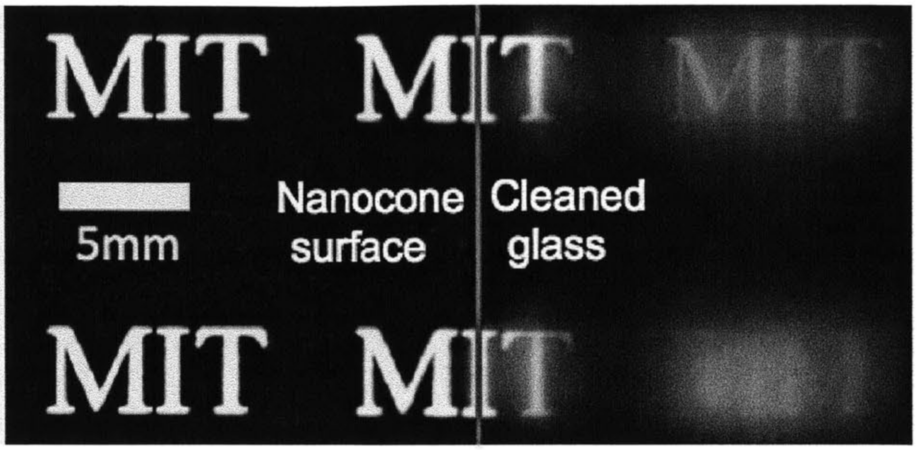

Figure 3-9: Optical Image of printed letters through fogged nanocone (left) and cleaned glass (right) surfaces

In Figure 3-9, the clear image of white letters through the nanocone surface exhibits qualitatively sufficient anti-fogging property from structural superhydrophilicity, compared to the blurry image through a glass slide, which is originally hydrophilic.

To further investigate the time dependent response of effect on fogging, I measured the transmission as shown in Figure 3-9. Relative humidity (RH) and temperature (T) were measured for rigorous experiments. Before the optical measurement, the temperature of both the nanotextured surface and glass slide for 5 minutes inside a refrigerator (T = 8.3 ± 0.4°C, RH = 43.0 ± 2.0%). Fog generation was facilitated by the application of boiling water below the samples for 5 seconds where the vertical distance between our sample and the liquid-air interface of boiling water was 5 cm (T = 37.5 ± 0.5°C, RH= 58.5 ± 1.5%). Then, each fogged surface was immediately introduced to the transmission measurement setup (T = 23.5 ± 0.5 °C, RH = 37.5 ± 0.5%). Three surfaces were applied at 20 seconds to the transmission experimental setup, and the slight decrease of the transmission at this moment because the edges of those surfaces block and scatter the incident laser when the surfaces was placed into the experimental setup. The initial transmission values of three different surfaces before introducing the surfaces into the measurement setup are similar, whereas the transmission of the fogged cleaned glass slide plummets and then increases to the lower saturated value ($\simeq$ 92%) compared to that of the nanocone surface ($\simeq$ 98%),

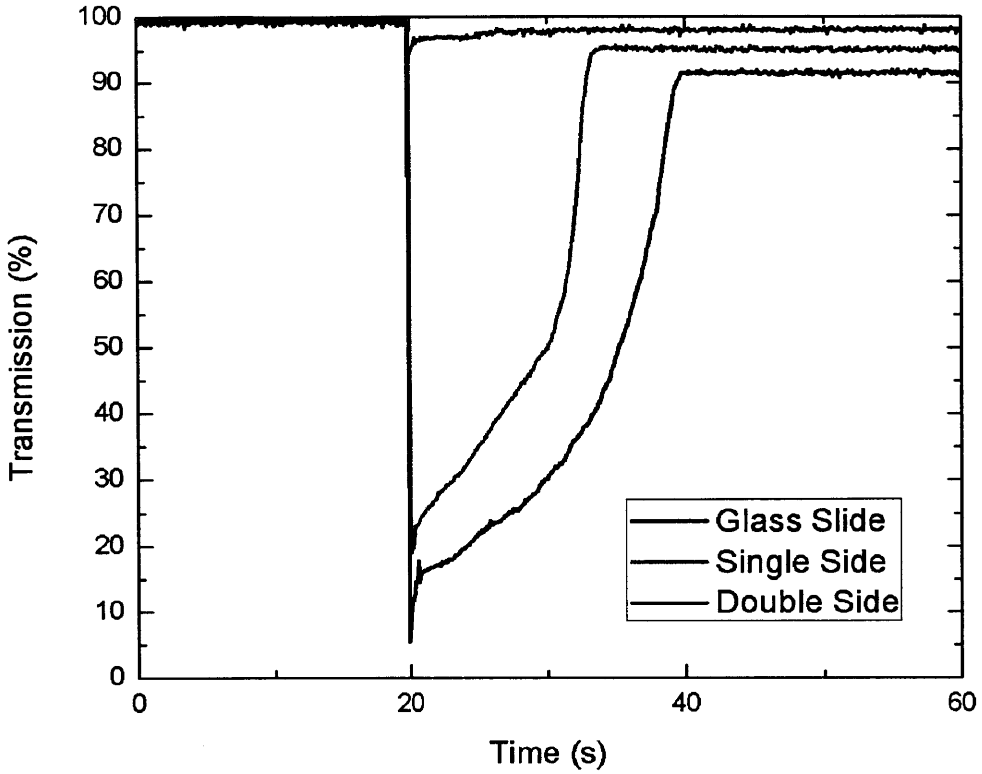

Figure 3-10: Transient response of optical transmission due to fogging on double-side patterned fused silica (blue line), single-side patterned one (red line), and glass (black line) surfaces

which means loss of transmission due to the generation and disappearance of fog and intrinsic reflection on the glass slide. From the experiment, the double-side patterned sample doesn't possess any fogging on its both surfaces, and acquires over 92% transparency all the time.

3.6 Conclusion

By developing multiple shrinking mask etching for large-area patterning on silicon oxide substrate, subwavelength high aspect ratio nanocone structures providing enhanced transmission (or anti-reflective) and superhydrophobic/philic properties were demonstrated. By texturing a square array of nanocones on both sides of the substrate and modifying its surface energy with silanization, it is possible to combine robust superhydrophobicity and enhanced transparency (or anti-reflective property) into one surface. In addition to the synergetic effect, water vapor condensation experiment has confirmed the possibility of macroscopic anti-fogging function of nanocone structure for practical applications including transparent windshields and goggles, which are self-cleaning outside.

For further plan, fabrication of the subwavelength high aspect ratio nanocone structures through nanoimprint method [44] will be investigated and developed. If these surfaces are able to be fabricated with transparent polymers such as PDMS and PMMA, a new possibility for producing these at low costs for commercial-scale manufacture will be shown in the future.

Chapter 4

Fabrication of Dielectric Aperiodic Nanostructured Luneburg Lens in Optical Frequencies

4.1 Introduction

A Luneburg lens is a type of gradient index (GRIN) elements which generates diffraction-limited focus at the edge of its opposite to an incident plane wave. The nanostructured Luneburg lens at optical frequencies using aperiodic photonic nanostructures was fabricated.

4.2 Luneburg Lens

Luneburg lens was proposed by Rudolf Karl Luneburg in 1944 [45] for the first time as a lens with a specific index distribution where a plane wave propagating through the lens makes a focal point at the edge of the lens. Figure 4-1 shows the schematic of the Luneburg lens. The refractive index distribution of the lens is

$$n(r) = n_0\sqrt{2 - \left(\frac{r}{R}\right)^2} \tag{4.1}$$

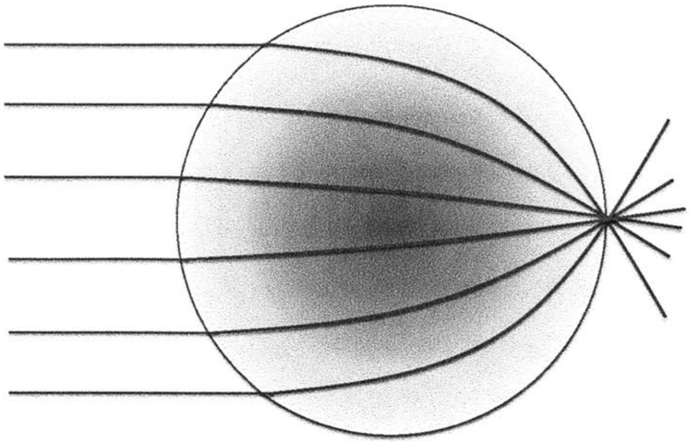

Figure 4-1: Schematic of Luneburg lens with a propagating plane wave making a focus at the opposite edge of the lens.

where n_0 is the index of the surrounding medium, R is the radius of the lens, and r is the distance from any point to the center of the lens. The index of the surrounding medium is a constant, n_0, and the index inside lens decreases gradually from $n_0\sqrt{2}$ and n_0. Since the index distribution is spherically symmetric [46], any incoming plane wave with any direction converges on a single point on the edge of the lens. Due to its unique focusing property, it has been used for focusing signals such as microwaves [47, 48, 49]. In optical frequency region, however, it is hard to achieve gradient index distribution given by Luneburg lens. In this chapter, fabrication process of the Luneburg lens for operation at near infrared optical frequencies is presented and the fabrication result is shown.

4.3 Fabrication Process

Based on the design of the structures [46], the Luneburg lens consisting of silicon rods was fabricated by a scanning electron–beam lithography system (RAITH 150). Required refractive index distribution is achieved by subwavelength silicon rod structures which diameters varies, as depicted in Figure 4-2. When the variation in the dimension of structures is slow enough to be considered periodic within the adiabatic length scale, index distribution can be determined and controlled by local dispersion relations through established photonic crystal theory [50, 51].

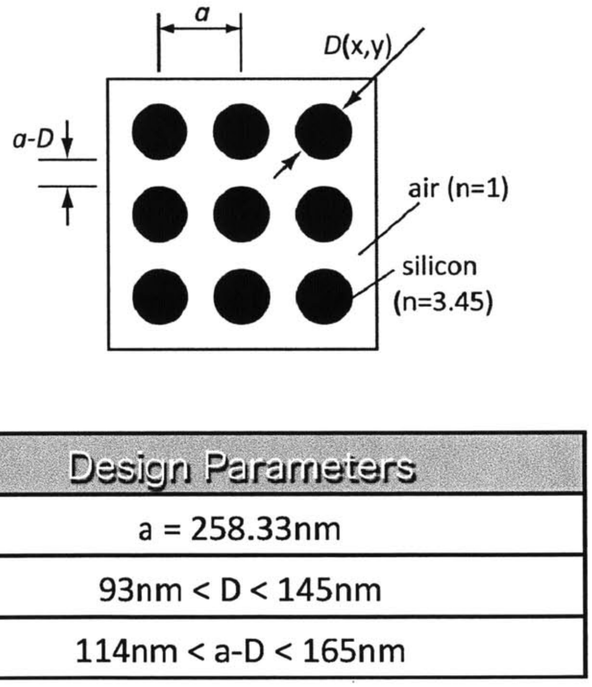

Design Parameters
a = 258.33nm
93nm < D < 145nm
114nm < a-D < 165nm

Figure 4-2: Design parameters on the Luneburg lens [46]

Figure 4-3 demonstrates the fabrication process. A silicon-on-insulator (SOI) wafer with device layer thickness of 340nm and oxide layer thickness of 1μm was prepared. After RCA cleaning, 100nm-thick-hydrogen silsequioxane (HSQ) film was spun on the SOI wafer, and was then exposed with the scanning electron-beam lithography system.

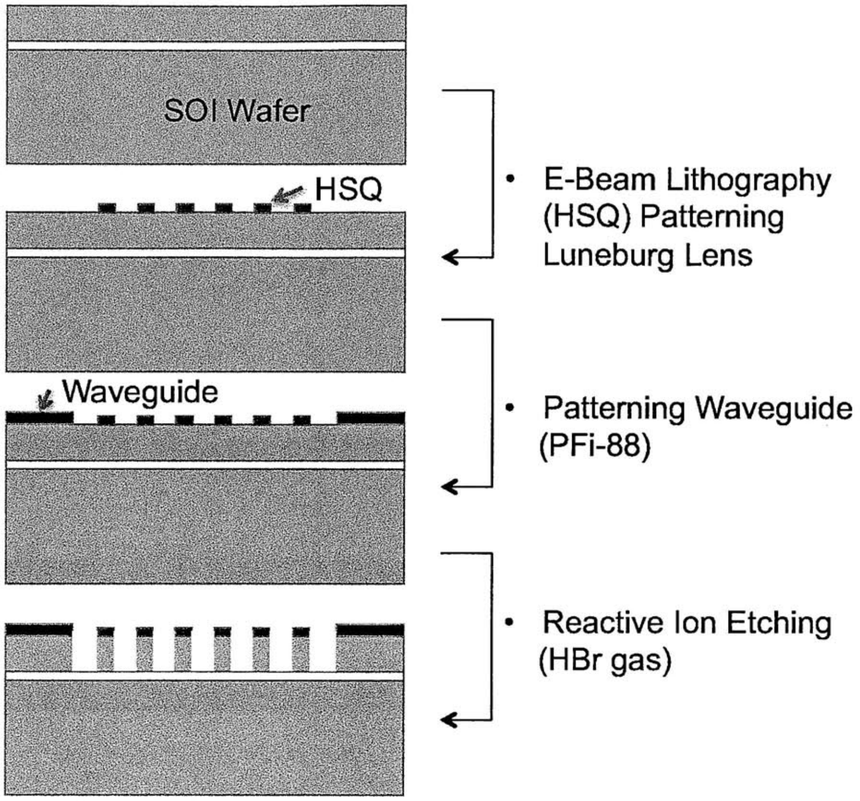

Figure 4-3: Fabrication process of a Luneburg lens with waveguide

In order to avoid proximity effect in electron–beam lithography [52], rods were drawn by a single electron beam in a spiral as shown in Figure 4-4.

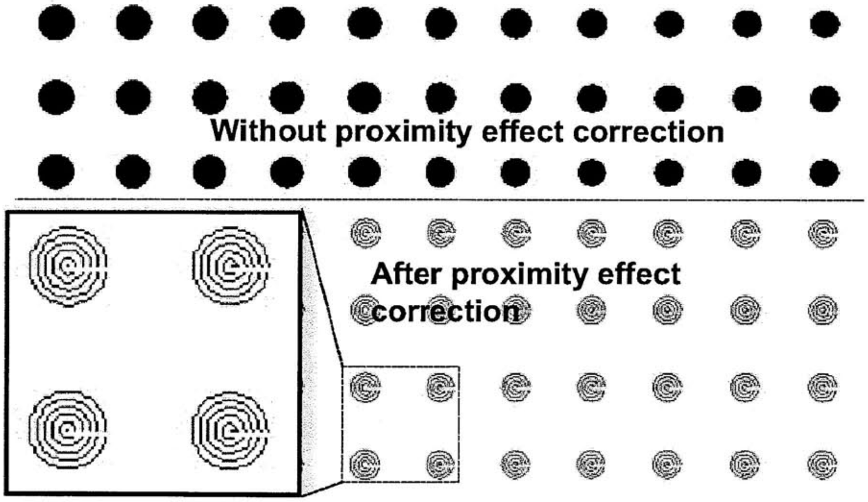

Figure 4-4: Schematic of proximity effect correction (Electron–beam lithography)

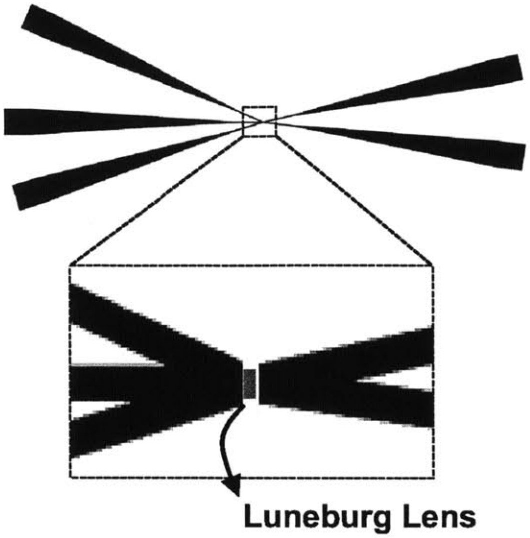

Figure 4-5: Schematic of waveguide and the fabricated Luneburg lens

Unexposed HSQ was removed with a salty developer [53], and exposed HSQ remain as posts on top of the wafer. The remaining HSQ was annealed to enhance adhesion with substrate at 950 °C for 2 minutes by Rapid Thermal Annealer (AG Associates Heatpulse 410).

In order to verify its capability to focus an incoming plane wave from any incident angle to a point on the edge at the other side of the lens, the waveguides were fabricated before reactive ion etching process. Figure 4-5 show a schematic of waveguide and the fabricated Luneburg lens. PFi-88 positive photoresist was spun on top of the sample and patterned with optical lithography, as shown in the Figure 4-6 and Figure 4-7. Then, the silicon layer is etched with reactive ion etching (RIE) by hydrogen bromide (HBr) gas, and the Luneburg lens was finally created. All the fabrication processes are described in Table A.2.

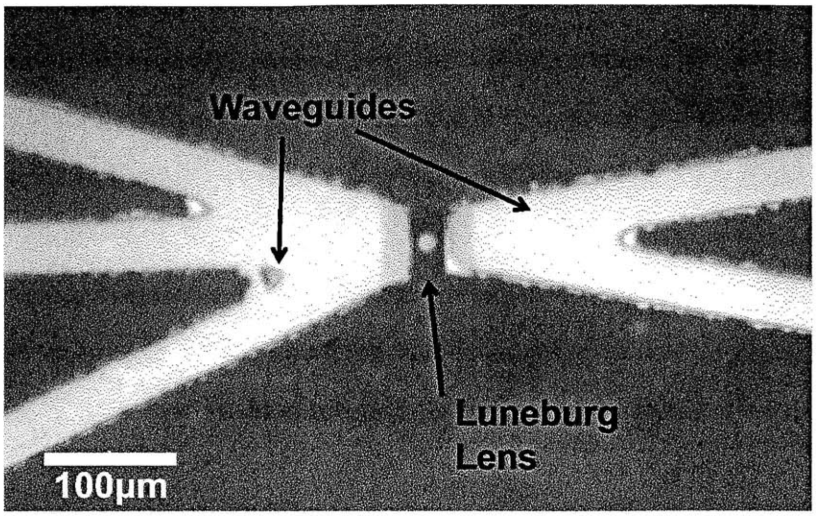

Figure 4-6: Optical Image of Fabricated Waveguides surrounding Luneburg lens

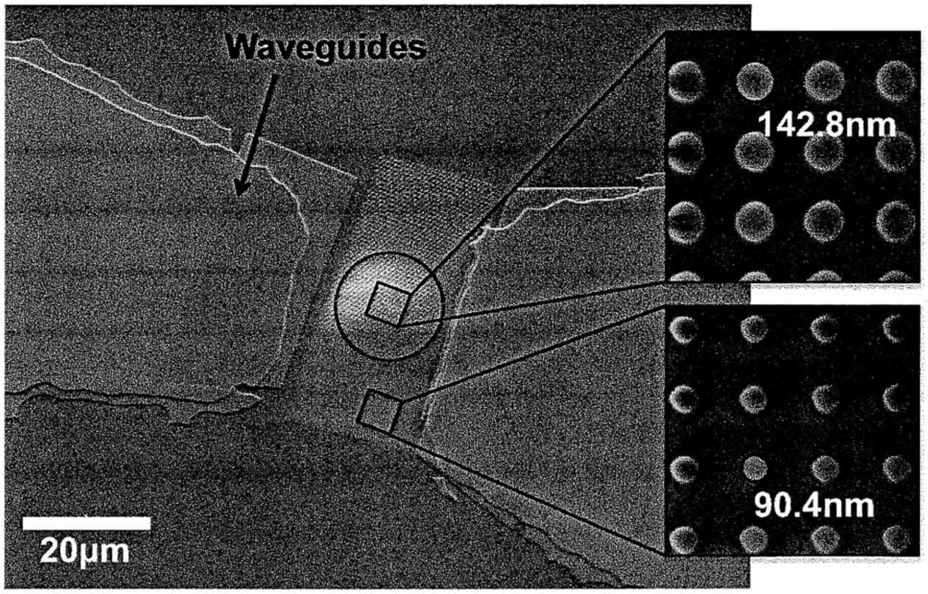

Figure 4-7: SEM micrograph of the fabricated Luneburg lens structures. The period of the lattice is 258nm, and the overall size of the nanostructure region is 50μm by 20μm. Waveguides for coupling light into the structure can be seen on the left and right of the structure [46].

4.4 Future Work

In this chapter, the fabrication of the aperiodic nanostructured Luneburg lens designed in optical frequency region and its result are shown. The performance of the fabricated Luneburg lens will be optically tested with a laser of its wavelength of λ $=1.55$ μm.

Appendix A

Fabrication Processes

All fabrication of nanocone structures and optical components were conducted in the Nano Structure Laboratory (NSL), Microsystems Technology Lab (MTL), the Space Nanotechnology Laboratory (SNL), and Scanning Electron Beam Lithography (SEBL) facility at the Massachusetts Institute of Technology (MIT). The detailed fabrication processes are described.

A.1 Fabrication Process of Subwavelength Periodic High Aspect Ratio Nanocone Structures

All the fabrication process is described in Table A.1. The fabrication process in Table A.2.1 was started with a 6-inch UV-graded fused silica wafer. The machine column refers to the machine that has been used in the Nanostructure Laboratory (NSL) at MIT unless otherwise noted.

Table A.1: Fabrication Process of subwavelength periodic high aspect ratio nanocone structures

Step	Description	Recipe	Machine
1	RCA cleaning		acid hood (MTL)
2	Deposition of polysilicon	240 nm (both sides)	CVD (MTL)
3	RCA cleaning		acid hood (MTL)
4	spin resist (S1813)	4 μm on both sides	spinner
5	dicing	45mm by 45mm	diesaw machine (MTL)
6	resist strip	NMP	wet bench
7	RCA cleaning		acid hood
8	sonication	5 minutes	ultrasonic bath
9	spin HSQ	340 nm on both sides	spinner
10	baking	11 hours at 500 °C	oven (SNL)
11	RCA cleaning		acid hood
12	sonication	5 minutes	ultrasonic bath
13	plasma oxygen etching		RIE
14	spin ARC (I-con 7)	105 nm on both sides	spinner
15	bake	1 hour at 180°C	oven
16	spin resist (PFi-88)	105 nm on the front side	spinner

Continued on next page

Table A.1 – continued from previous page

Step	Description	Recipe	Machine
16	spin resist (S1813)	4 μm on the back side	spinner
17	bake	60 seconds at 90°C	hot plate
18	expose	PFi-88	Lloyd's mirror
19	develop	CD-26	wet bench
20	plasma oxygen etching		RIE
21	plasma CHF_3 etching		RIE
22	plasma oxygen etching		RIE
23	plasma CF_4 etching		RIE
24	plasma HBr etching		RIE (SNL)
25	plasma CHF_3 etching		RIE
26	RCA cleaning		acid hood
27	spin resist (S1813)	4 μm on the front side	spinner
28	spin ARC (I-con 7)	105 nm on back side	spinner
29	bake	60 seconds at 180°C	hot plate
30	spin resist (PFi-88)	105 nm on the back side	spinner
31	bake	60 seconds at 90°C	hot plate
32	expose	PFi-88	Lloyds mirror

Continued on next page

Table A.1 – continued from previous page

Step	Description	Recipe	Machine
33	develop	CD-26	wet bench
34	plasma oxygen etching		RIE
35	plasma CHF_3 etching		RIE
36	plasma oxygen etching		RIE
37	plasma CF_4 etching		RIE
38	plasma HBr etching		RIE (SNL)
39	plasma CHF_3 etching		RIE
40	RCA cleaning		acid hood
41	TMAH etching	1 minute	acid hood

A.2 Fabrication Process of the Dielectric Aperiodic Nanostructured Luneburg Lens

The machine column refers to the machine that has been used in the Nanostructure Laboratory (NSL) at MIT unless otherwise noted.

Table A.2: Fabrication Process of the dielectric aperiodic nanostructured Luneburg lens [46]

Step	Description	Recipe	Machine
1	RCA clean		acid hood
2	spin HSQ		spinner
3	evaporate Al	3-5 nm	e-beam evaporator (MTL)
4	e-beam pattern		Raith 150 (SEBL)
5	develop	NaOH + NaCl[53]	wet bench
6	rinse and dry		wet bench
7	Annealing	2 minutes at 950°C	Rapid Thermal Annealer (MTL)
8	spin resist (PFi-88)		spinner
9	bake	90 seconds at 90°	hot plate
10	expose	waveguide pattern	OAI
11	develop	CD-26	wet bench
12	rinse and dry		wet bench

Bibliography

[1] CLAPHAM, P. B. and HUTLEY, M. C., "Reduction of Lens Reflexion by the Moth Eye Principle," *Nature*, Vol. 244, No. 5414, Aug. 1973, pp. 281–282.

[2] Wenzel, R. N., "RESISTANCE OF SOLID SURFACES TO WETTING BY WATER," *Industrial & Engineering Chemistry*, Vol. 28, No. 8, Aug. 1936, pp. 988–994.

[3] Cassie, A. B. D. and Baxter, S., "Wettability of porous surfaces," *Transactions of the Faraday Society*, Vol. 40, Jan. 1944, pp. 546–551.

[4] Huang, Y. F., Chattopadhyay, S., Jen, Y. J., Peng, C. Y., Liu, T. A., Hsu, Y. K., Pan, C. L., Lo, H. C., Hsu, C. H., Chang, Y. H., Lee, C. S., Chen, K. H., and Chen, L. C., "Improved broadband and quasi-omnidirectional anti-reflection properties with biomimetic silicon nanostructures," *Nature nanotechnology*, Vol. 2, No. 12, 2007, pp. 770–774.

[5] Lafuma, A. and Quere, D., "Superhydrophobic states," *Nature materials*, Vol. 2, No. 7, 2003, pp. 457–460.

[6] Quéré, D., "Wetting and Roughness," *Annual Review of Materials Research*, Vol. 38, No. 1, Aug. 2008, pp. 71–99.

[7] Bhushan, B., "Biomimetics: lessons from nature–an overview," *Philosophical transactions. Series A, Mathematical, physical, and engineering sciences*, Vol. 367, No. 1893, 2009, pp. 1445–1486.

[8] Liu, K. and Jiang, L., "Bio-inspired design of multiscale structures for function integration," *Nano Today*, Vol. 6, No. 2, 2011, pp. 155–175.

[9] Zhai, L., Berg, M. C., Cebeci, F. C., Kim, Y., Milwid, J. M., Rubner, M. F., and Cohen, R. E., "Patterned superhydrophobic surfaces: toward a synthetic mimic of the Namib Desert beetle." *Nano letters*, Vol. 6, No. 6, June 2006, pp. 1213–7.

[10] Southwell, W. H., "Gradient-index antireflection coatings," *Optics Letters*, Vol. 8, No. 11, Nov. 1983, pp. 584.

[11] Grann, E. B., Varga, M. G., and Pommet, D. A., "Optimal design for antireflective tapered two-dimensional subwavelength grating structures," *Journal of the Optical Society of America A*, Vol. 12, No. 2, Feb. 1995, pp. 333.

[12] Vukusic, P. and Sambles, J. R., "Photonic structures in biology," *Nature*, Vol. 424, No. 6950, Aug. 2003, pp. 852–855.

[13] Xi J.-Q., Schubert, M. F., Kim, J. K., Schubert, E. F., Chen, M., Lin, S.-Y., LiuW., and A., S., "Optical thin-film materials with low refractive index for broadband elimination of Fresnel reflection," *Nat Photon*, Vol. 1, No. 3, March 2007, pp. 176–179.

[14] Yamada, K., Umetani, M., Tamura, T., Tanaka, Y., Kasa, H., and Nishii, J., "Antireflective structure imprinted on the surface of optical glass by SiC mold," *Applied Surface Science*, Vol. 255, No. 7, 2009, pp. 4267–4270.

[15] Kanamori, Y., Sasaki, M., and Hane, K., "Broadband antireflection gratings fabricated upon silicon substrates," *Optics Letters*, Vol. 24, No. 20, Oct. 1999, pp. 1422.

[16] Sainiemi, L., Jokinen, V., Shah, A., Shpak, M., Aura, S., Suvanto, P., and Franssila, S., "Non-reflecting silicon and polymer surfaces by plasma etching and replication." *Advanced materials (Deerfield Beach, Fla.)*, Vol. 23, No. 1, Jan. 2011, pp. 122–6.

[17] Sun, C.-H., Jiang, P., and Jiang, B., "Broadband moth-eye antireflection coatings on silicon," *Applied Physics Letters*, Vol. 92, No. 6, Feb. 2008, pp. 061112.

[18] Zhu, J., Hsu, C. M., Yu, Z. F., Fan, S. H., and Cui, Y., "Nanodome Solar Cells with Efficient Light Management and Self-Cleaning," *Nano Letters*, Vol. 10, No. 6, 2010, pp. 1979–1984.

[19] Zorba, V., Stratakis, E., Barberoglou, M., Spanakis, E., Tzanetakis, P., Anastasiadis, S. H., and Fotakis, C., "Biomimetic Artificial Surfaces Quantitatively Reproduce the Water Repellency of a Lotus Leaf," *Advanced Materials*, Vol. 20, No. 21, Nov. 2008, pp. 4049–4054.

[20] Koch, K., Bhushan, B., and Barthlott, W., "Multifunctional surface structures of plants: An inspiration for biomimetics," *Progress in Materials Science*, Vol. 54, No. 2, 2009, pp. 137–178.

[21] Parker, A. R. and Lawrence, C. R., "Water capture by a desert beetle." *Nature*, Vol. 414, No. 6859, Nov. 2001, pp. 33–4.

[22] Howarter, J. A. and Youngblood, J. P., "Self-Cleaning and Next Generation Anti-Fog Surfaces and Coatings," *Macromolecular Rapid Communications*, Vol. 29, No. 6, March 2008, pp. 455–466.

[23] Patel, P., Choi, C. K., and Meng, D. D., "Superhydrophilic Surfaces for Antifogging and Antifouling Microfluidic Devices," *Journal of the Association for Laboratory Automation*, Vol. 15, No. 2, 2010, pp. 114–119.

[24] Huang, Y.-F., Chattopadhyay, S., Jen, Y.-J., Peng, C.-Y., Liu, T.-A., Hsu, Y.-K., Pan, C.-L., Lo, H.-C., Hsu, C.-H., Chang, Y.-H., Lee, C.-S., Chen, K.-H., and Chen, L.-C., "Improved broadband and quasi-omnidirectional anti-reflection properties with biomimetic silicon nanostructures." *Nature nanotechnology*, Vol. 2, No. 12, Dec. 2007, pp. 770–4.

[25] Wu, C.-T., Lin, C.-H., Cheng, C., Wu, C.-S., Ting, H.-C., Chang, F.-C., and Ko, F.-H., "Design of Artificial Hollow Moth-Eye Structures Using Anodic Nanocones for High-Performance Optics," *Chemistry of Materials*, Vol. 22, No. 24, 2010, pp. 6583–6589.

[26] Su, C., Li, J., Geng, H., Wang, Q., and Chen, Q., "Fabrication of an optically transparent super-hydrophobic surface via embedding nano-silica," *Applied Surface Science*, Vol. 253, No. 5, 2006, pp. 2633–2636.

[27] Choi, K., Park, S. H., Song, Y. M., Lee, Y. T., Hwangbo, C. K., Yang, H., and Lee, H. S., "Nano-tailoring the Surface Structure for the Monolithic High-Performance Antireflection Polymer Film," *Advanced Materials*, Vol. 22, No. 33, 2010, pp. 3713–3718.

[28] Gao, X., Yan, X., Yao, X., Xu, L., Zhang, K., Zhang, J., Yang, B., and Jiang, L., "The Dry-Style Antifogging Properties of Mosquito Compound Eyes and Artificial Analogues Prepared by Soft Lithography," *Advanced Materials*, Vol. 19, No. 17, 2007, pp. 2213–2217.

[29] Martines, E., Seunarine, K., Morgan, H., Gadegaard, N., Wilkinson, C. D. W., and Riehle, M. O., "Superhydrophobicity and superhydrophilicity of regular nanopatterns." *Nano letters*, Vol. 5, No. 10, Oct. 2005, pp. 2097–103.

[30] Song, Y. M., Choi, H. J., Yu, J. S., and Lee, Y. T., "Design of highly transparent glasses with broadband antireflective subwavelength structures," *Optics Express*, Vol. 18, No. 12, June 2010, pp. 13063.

[31] Tuteja, A., Choi, W., Mabry, J. M., McKinley, G. H., and Cohen, R. E., "Robust omniphobic surfaces." *Proceedings of the National Academy of Sciences of the United States of America*, Vol. 105, No. 47, Nov. 2008, pp. 18200–5.

[32] Korre, H., Fucetola, C. P., Johnson, J. A., and Berggren, K. K., "Development of a simple, compact, low-cost interference lithography system," *Journal of Vacuum Science & Technology B: Microelectronics and Nanometer Structures*, Vol. 28, No. 6, 2010, pp. C6Q20.

[33] Chang, C.-H., *Multilevel interference lithography–fabricating sub-wavelength periodic nanostructures*, Ph.D. thesis, Massachusetts Institute of Technology, 2008.

[34] Smith, H. I., "Low cost nanolithography with nanoaccuracy," *Physica E: Low-dimensional Systems and Nanostructures*, Vol. 11, No. 2-3, 2001, pp. 104–109.

[35] OReilly, T. B. and Smith, H. I., "Linewidth uniformity in Lloyds mirror interference lithography systems," *Journal of Vacuum Science & Technology B: Microelectronics and Nanometer Structures*, Vol. 26, No. 6, 2008, pp. 2131.

[36] Kern, W., "The Evolution of Silicon Wafer Cleaning Technology," *Journal of The Electrochemical Society*, Vol. 137, No. 6, June 1990, pp. 1887–1892.

[37] Liou, H.-C. and Pretzer, J., "Effect of curing temperature on the mechanical properties of hydrogen silsesquioxane thin films," *Thin Solid Films*, Vol. 335, No. 1-2, 1998, pp. 186–191.

[38] Hehl, K. and Wesch, W., "Calculation of optical reflection and transmission coefficients of a multi-layer system," *Physica Status Solidi (a)*, Vol. 58, No. 1, March 1980, pp. 181–188.

[39] Sonphao, W. and Chaisirikul, S., *Silicon anisotropic etching of TMAH solution*, IEEE.

[40] Moharam, M. G. and Gaylord, T. K., "Rigorous coupled-wave analysis of planar-grating diffraction," *Journal of the Optical Society of America*, Vol. 71, No. 7, July 1981, pp. 811.

[41] Moharam, M. G., Grann, E. B., Pommet, D. A., and Gaylord, T. K., "Formulation for stable and efficient implementation of the rigorous coupled-wave analysis of binary gratings," *Journal of the Optical Society of America A*, Vol. 12, No. 5, May 1995, pp. 1068.

[42] Moharam, M. G., Pommet, D. A., Grann, E. B., and Gaylord, T. K., "Stable implementation of the rigorous coupled-wave analysis for surface-relief gratings: enhanced transmittance matrix approach," *Journal of the Optical Society of America A*, Vol. 12, No. 5, May 1995, pp. 1077.

[43] Quéré, D., "Non-sticking drops," *Reports on Progress in Physics*, Vol. 68, No. 11, Nov. 2005, pp. 2495–2532.

[44] Chou, S. Y., Krauss, P. R., and Renstrom, P. J., "Imprint Lithography with 25-Nanometer Resolution," *Science*, Vol. 272, No. 5258, April 1996, pp. 85–87.

[45] Luneburg, R. K., *Mathematical theory of optics*, University of California Press, 1964.

[46] Takahashi, S., *Design and Fabrication of micro- and nano-dielectric structures for imaging and focusing at optical frequencies*, Ph.D. thesis, Massachusetts Institute of Technology, 2011.

[47] Gunderson, L. C. and Holmes, G. T., "Microwave Luneburg Lens," *Applied Optics*, Vol. 7, No. 5, May 1968, pp. 801.

[48] Schoenlinner, B., Ebling, J., Eleftheriades, G., and Rebeiz, G., "Wide-scan spherical-lens antennas for automotive radars," *IEEE Transactions on Microwave Theory and Techniques*, Vol. 50, No. 9, Sept. 2002, pp. 2166–2175.

[49] Rondineau, S., Himdi, M., and Sorieux, J., "A sliced spherical Luneburg lens," *Antennas and Wireless Propagation Letters*, Vol. 2, No. 11, 2003, pp. 163–166.

[50] Joannopoulos, J. D., Johnson, S. G., Winn, J. N., and Meade, R. D., *Photonic Crystals Molding the Flow of Light*, Princeton University Press, 2008.

[51] Satoshi Takahashi, Chih-Hao Chang, Se-Young Yang, Hyungryul J. Choi, and George Barbastathis, "Fabrication of Dielectric Aperiodic Nanostructured Luneburg Lens in Optical Frequencies - OSA Technical Digest (CD)," *Quantum Electronics and Laser Science Conference*, Optical Society of America, May 2011, p. QTuM2.

[52] Chang, T. H. P., "Proximity effect in electron-beam lithography," *Journal of Vacuum Science and Technology*, Vol. 12, No. 6, Nov. 1975, pp. 1271.

[53] Yang, J. K. W. and Berggren, K. K., "Using high-contrast salty development of hydrogen silsesquioxane for sub-10-nm half-pitch lithography," *Journal of Vacuum Science & Technology B: Microelectronics and Nanometer Structures*, Vol. 25, No. 6, 2007, pp. 2025.